# Assimilation of wide-swath altimetry observations to correct large-scale river routing model parameters

Charlotte Marie Emery[1,2], Sylvain Biancamaria[1], Aaron Boone[3], Sophie Ricci[4], Mélanie C. Rochoux[4], Vanessa Pedinotti[5], and Cédric H. David[2]

[1]LEGOS, 16 Avenue Edouard Belin, 31400 Toulouse, France.
[2]Jet Propulsion Laboratory, California Institute of Technology, Pasadena, CA, USA
[3]CNRM-GAME, Meteo-France, 42 Avenue Gaspard Coriolis, 31000 Toulouse, France
[4]CECI, Université de Toulouse, CERFACS, CNRS, 42 Avenue Gaspard Coriolis, 31057 Toulouse cedex 1, France
[5]Magellium, 1 Rue Ariane, 31520 Ramonville-Saint-Agne, France

**Correspondence:** Charlotte Marie Emery (charlotte.emery@jpl.nasa.com)

**Abstract.** Land surface models combined with river routing models are widely used to study the continental part of the water cycle. They give global estimates of water flows and storages but not without non-negligible uncertainties; among which inexact input parameters have a significant part. The incoming Surface Water and Ocean Topography (SWOT) satellite mission, with a launch schedule for 2021, will be dedicated to measure water surface elevations, widths and surface slopes of rivers larger than 100 meters at global scale. SWOT will provide a significant amount of new data for river hydrology and they could be combined, through data assimilation, to global-scale models in order to correct their input parameters and reduce their associated uncertainty. The objective of this study is to present a data assimilation platform based on the asynchronous ensemble Kalman filter (AEnKF) that assimilates synthetical SWOT observations of water elevations to correct the input parameters of a large scale hydrologic model over a 21-day time window. The study is applied on the ISBA-CTRIP model over the Amazon basin and focuses on correcting the spatial distribution of the river Manning coefficients. The data assimilation algorithm, tested through a set of Observing System Simulation Experiments (OSSE), is able to retrieve the true value of the Manning coefficients within one assimilation cycle most of the time and shows perspectives in tracking the Manning coefficient temporal variations. Ultimately, in order to deal with potential bias between the observed and the model bathymetry, the assimilation of water elevation anomalies was also tested and showed promising results.

## 1 Introduction

Global Hydrological Models (GHM) are extensively exploited to study the continental component of the global water cycle (Doll et al., 2015; Sood and Smakhtin, 2015). Such models have been extensively developed over the past two decades in order to quantify freshwater flows and storage changes over continental surfaces (Bierkens, 2015). Those models are based on the coupling of a Land Surface Model (LSM) with a River Routing Model (RRM). As an example, the ISBA-CTRIP (Decharme et al., 2019) hydrologic model results from the coupling of the ISBA LSM (Noilhan and Planton, 1989) and the TRIP RRM (Oki and Sud, 1998). LSMs simulate the energy and water balance at the interface soil-atmosphere-vegetation while RRMs

emulate the lateral transfer of freshwater toward the continent-ocean interface. More particularly, the current study focuses on the river component of the terrestrial water cycle simulated by RRM.

GHMs give a global view of the state of the water flow and storage at the model spatial and temporal resolutions. However, there are multiple sources of model uncertainties such as the model structure, the external forcing and the input parameters
5   (Liu and Gupta, 2007; Renard et al., 2010). Model structure uncertainties initially arose from a lack of knowledge in the hydrologic processes or from simplifying assumptions made to limit simulation computational cost. However, with the increase of computational power, models are more and more complex (Liu and Gupta, 2007; Melsen et al., 2016): they run at finer spatial resolution, they include new physical processes and use an increasing number of fully distributed forcing and parameter datasets (Liu et al., 2012). Inevitably, reducing the model structure uncertainty causes an increase in the number of model
10  input parameters and potentially inflates the model uncertainty in those parameters. Input parameters express the spatial and/or temporal properties of the system. However, for parameters measurable on the field, their spatial scale may differ from the model scale while other conceptual parameters are not even directly observable and measurable on the field (Moradkhani et al., 2005; Melsen et al., 2016) and are inferred using geomorphological empirical formula and/or indirect method such as calibration (Gupta et al., 1998; Beven, 2012).

15  Another way to study the terrestrial water cycle is to use direct observations of this system. Most parts of the terrestrial water cycle are currently observed and measured from in situ or remote techniques (Sanoo et al., 2011; Vinukollu et al., 2011; Rodell et al., 2015). For the observations of rivers, in situ techniques measure river water elevations at gauge stations. In situ measurements are commonly very accurate and also frequent (i.e. sub-daily) but their main limitation is their spatially sparse sampling and their decreasing number over the last decades at global scale (International Association of Hydrological Sciences
20  Ad Hoc Group on Global Water Sets et al., 2001). Coincidentally, remotely-sensed data provided by satellite missions have quite increased since the 90's and deliver effective river observations. The most unequivocal instrument operating to assess river water levels remains the nadir altimeter. Nadir altimetry gives localized water elevation measurements along the satellite ground track. Initially, altimeters were designed to monitor ocean topography but they were broadened to the observation of lakes (Cretaux et al., 2009), floodplains (Birkett et al., 2002) and later on, rivers (Silva et al., 2010). However, their main
25  limitation remains their limited spatial and temporal samplings: generally several days between two consecutive measurements at a limited number of locations. Besides, over continental surfaces, the signal is not always retrievable or with important vertical error. Therefore, current river observations provide a more accurate view of the river system than models but they are quite limited by their sparse availability in space and time.

However, the incoming Surface Water and Ocean Topography (SWOT) mission, jointly developed by NASA, CNES, CSA
30  and UKSA and scheduled for a launch in 2021, will be dedicated to the observation of continental free surface water with a better spatial and temporal coverage than the current nadir missions (such as EnviSat, the JASON series or also Sentinel-3A/B). SWOT main payload called KaRIn, for Ka-band Radar INterferometer (Fj$'$ortoft et al., 2014), will observe surfaces under two swaths of 50 km each separated by a nadir-gap of 20 km and will have a near-global coverage. For hydrology, SWOT will observe rivers wider than 100 meters as well as lakes and wetlands larger than $250 \times 250$ m$^2$ within the latitudes 78° South and
35  78° North and with a repetitivity of 21 days. SWOT will provide two-dimensional images of water surface elevations with a

vertical accuracy of 10 cm when averaged over 1 km$^2$ of water area. Along with water surface elevation measurements in rivers, SWOT will also provide observations of river width, surface slope and estimates of discharge based on SWOT observations. SWOT will provide a significant amount of new data for surface hydrology. It will give an ensemble of constraints that will allow a better depiction of surface water in hydrological models. Those new data could be combined or integrated to global-

5 scale hydrological model in order to correct them and improve their performances and forecasting capabilities.

Data assimilation techniques are a set of mathematical methods to combine a physical model and related external measurements while encompassing their uncertainties. Data assimilation aims at improving the model ability to forecast and/or emulate the physical system evolution. For this purpose, data assimilation methods are built to correct either the model's outputs (state estimation) or the model's input parameters (parameter estimation or PE), sometimes both simultaneously. Data assimilation

10 for state estimation has been widely applied in meteorology and oceanography, and is more and more developed for large-scale terrestrial hydrology (Clark et al., 2008; Michailovsky et al., 2013; Paiva et al., 2013; Emery et al., 2018). Data assimilation for PE in hydrology has been initially developed as a dynamic alternative to model calibration (Montzka et al., 2011; Panzeri et al., 2013; Ruiz et al., 2013; Shi et al., 2015). In most models, parameters are assumed constant in time while, in reality, they may vary seasonally or under evolving climate and/or anthropogenic conditions. Therefore, sequential data assimilation can

15 help track model parameters variations in time (Kurtz et al., 2012; Deng et al., 2016; Pathiraja et al., 2016). For example, PE is used to retrieve conceptual parameters of hydrologic models such as friction coefficients (Pedinotti et al., 2014; Oubanas et al., 2018; Hafliger et al., 2019) or residence time of quick- and slow-flow reservoirs and partition of runoff excess (Vrugt et al., 2012; Pathiraja et al., 2016).

Before launch, in the preparatory phase, Observing System Simulation Experiments (OSSE) can be done to assess the

20 benefits from assimilating SWOT data into a hydrological model. More particularly, several studies focus on the possibility of using SWOT data to retrieve critical river parameters such as the river bathymetry (Durand et al., 2008; Yoon et al., 2012; Mersel et al., 2013) and/or the riverbed roughness/friction coefficient (Pedinotti et al., 2014; Oubanas et al., 2018; Hafliger et al., 2019). In the present work, a data assimilation framework is used to correct input parameters of the large-scale ISBA-CTRIP model. More specifically, synthetical SWOT observations of water surface elevations are assimilated in order to correct the spatially-

25 distributed riverbed friction coefficients (or Manning coefficients). This choice was made following the results from the ISBA-CTRIP sensitivity analysis in Emery et al. (2016). In this preliminary study, the sensitivity of the simulated water elevations to several river input parameters (such as riverbed width, depth, slope and also friction coefficient) was evaluated. The results showed that the highest sensitivity was to the Manning coefficient. Furthermore, this study is built on the conclusions from Pedinotti et al. (2014) work: an Ensemble Kalman Filter (EnKF) is used (instead of the Extended Kalman Filter in Pedinotti

30 et al. (2014)) to better account for the nonlinearities of the system and better estimate the model errors. Also, Pedinotti et al. (2014) chose to update the Manning coefficient distribution at the grid cell scale and rose the question of equifinality (Beven and Freer, 2001) in the results. For the current study, it was decided to update the Manning coefficient distribution at a coarser regional scale identical to the one used in Emery et al. (2016). Finally, Pedinotti et al. (2014) used an assimilation window of 2 days. This configuration resulted in updated Manning coefficient time series displaying "unrealistic jumps" with a frequency

of about 20 days that were associated to the orbit repetitivity (longer than the 2-day window). Then, to avoid this phenomenon, the present study will use an assimilation window of 21 days corresponding to the current SWOT orbit repetitivity.

Section 2 will first give a description of the ISBA-CTRIP model used for this study. Then, Section 3 will present the particular data assimilation method developed for this study and finally, after presenting the assimilation strategy in Section 4, Sections 5 and 6 will give the data assimilation results.

## 2 Model

### 2.1 The ISBA-CTRIP large-scale hydrological model

The ISBA model (Noilhan and Planton, 1989) is a LSM defined at global-scale on a $0.5° \times 0.5°$ regular mesh grid that establishes the energy and water budget over the continental surfaces. This study operates the ISBA-3L version based on a three-layers soil (Boone et al., 1999). The budget equations are solved separately on every grid cell. Still, larger-scale spatial patterns in the radiative and precipitation forcing, the soil composition and the vegetation cover ensure spatial correlations between those cells. (for more details, see Decharme et al., 2012, 2019). In particular, ISBA gives a diagnostic of the surface runoff ($Q_{\text{ISBA,sur}}$) and the gravitational drainage ($Q_{\text{ISBA,sub}}$) later used as forcing inputs for the RRM denoted CTRIP.

The CTRIP model (Decharme et al., 2010, 2012, 2019), is defined on the same mesh grid as ISBA and follows a river netwok to laterally transfers water from one cell to another, down to the interface with the ocean (Oki and Sud, 1998). The study is based on the CTRIP version from Decharme et al. (2012) with three reservoirs, as illustrated in Figure 1a. The water mass [kg] stored in a groundwater reservoir $G$ and a floodplain reservoir $F$ interacts with the water mass in the surface reservoir $S$ representing the river. Only the surface reservoir $S$ is related to the river network and fills with the surface runoff $Q_{\text{ISBA,sur}}$, the outflow from upstream cells and the delayed drainage $Q_{\text{ISBA,sub}}$ by means of the groundwater reservoir. Occasionally, when the amount of water in the river exceeds a given threshold (defined by the water level in the reservoir), the river empties in the flooplains.

### 2.2 CTRIP parameters

Within a $0.5° \times 0.5°$ cell, the surface reservoir is an unique river channel that may gather multiples real river branches. Its rectangular cross-section is described by its slope $s$ [-], its width $W$ [m], its bankful depth $H_c$ [m], its length $L$ [m] and finally a Manning or friction coefficient $N$ [s m$^{-1/3}$] that assesses the reach resistance at the bottom of the river.

Each cell's elevation is deduced from the STN-30p Digital Elevation Model (http://daac.ornl.gov/ISLSCP_II/islscpii.shtml). These elevations are then compared to determine the riverbed slope $s$. Global empirical geomorphologic relationships are used to define the river width $W$ and bankful depth $H_c$. The arc length between grid cell centers, inflated by a meandering factor $\mu$, fixes the river reach length $L$. More details on these parameters can be found in Oki and Sud (1998) and Decharme et al. (2012).

The Manning coefficient $N$ is generally more complicated to estimate. Following Maidment (1993), it should take values between 0.025 and 0.03 for natural streams and values between 0.75 and 1 for smaller and mountainous tributaries and also floodplains. Therefore, global studies usually apply a constant Manning coefficient. However, it is ordinarily accepted that this parameter should vary in space and even in time over the river catchment. Consequently, CTRIP uses a spatially-distributed

5    Manning coefficient based on a simple linear relationship between the relative stream size in the current cell, denoted $SO$, and the size at the river mouth and the source cells, such that:

$$N = N_{min} + (N_{max} - N_{min}) \frac{SO_{max} - SO}{SO_{max} - SO_{min}}, \tag{1}$$

with $SO$ being the stream size relative measure at the current cell; $SO_{max} = 0.06$ the same measure at the river mouth and $SO_{min} = 0.04$ the measure at source cells (Decharme et al., 2012). The Manning coefficient is then set to be constant in time

10   while its spatial values decrease as the cells approaches the river outlet (following the river network).

All these parameters are eventually essential to estimate the spatially- and time-varying surface flow velocity $v(t)$ following the Manning formula (Manning, 1891):

$$v(t) = \frac{s^{\frac{1}{2}}}{N} \left( \frac{W h_S(t)}{W + 2 h_S(t)} \right)^{\frac{2}{3}}, \tag{2}$$

where $h_S$ is the river water depth estimated by

15   $$h_S = \frac{S}{\rho W L}, \tag{3}$$

and $\rho$ the water density. The flow velocity is ultimately used to estimate the discharge leaving the CTRIP cell:

$$Q_{\text{out}}^S(t) = \frac{v(t)}{L} S(t). \tag{4}$$

However, all these parameters have uncertainties because their true values are usely not known or also because most of these parameters are based on empirical relationships.

20   ## 2.3   CTRIP implementation over the Amazon basin

In this study, we present an OSSE test case over the Amazon river basin which hydrology is carefully described in Molinier et al. (1993); Wisser et al. (2010). This choice was motivated as the present work follows and complements studies over the same domain (Emery et al., 2016, 2018).

For ISBA-CTRIP, the Amazon basin is composed of a total number of 2028 cells. Based on the basin geomorphology

25   and hydrology (Meade et al., 1991), the basin has been split into 9 spatial regions. These zones, illustrated in Figure 1b, were initially introduced in (Emery et al., 2016) and will be re-exploited here. This subdivision will be used within the data assimilation platform to represent the spatially-distributed errors. For a detailed description of the zones, the reader can refer to (Emery et al., 2016).

## 2.4 ISBA-CTRIP forcing

For the present study, ISBA-CTRIP needs external atmospheric forcing to run. Similarly to Emery et al. (2016), such data are provided by the Global Soil Wetness Projet 3 (GSWP3, http://hydro.iis.u-tokyo.ac.jp/GSWP3) at a 3-hours time resolution. In the entire study, those forcing are considered perfect.

## 5 3 Method: Synthetic parameter estimation on ISBA-CTRIP

### 3.1 OSSE framework

In OSSE, we introduce beforehand a reference configuration for the model input parameters that we will consider thereafter as the *truth*. From those true parameters, we directly deduce the *true run* from a ISBA-CTRIP model integration. On the one hand, the synthetic observations used within data assimilation are obtained from perturbing the true observables (variables that are used as observations) using an error model that is representative of the real observation errors. On the other hand,
10 the control variables (the model variables to be corrected with data assimilation) first guess, at the beginning of the data assimilation experiment, are obtained by directly perturbing the true control variables. Control error also has to be chosen to be representative of the real modeling errors. OSSEs are prerequisite tests to ensure the implementation of the EnKF algorithm is correct and adapted to the hydrologic problem under consideration (temporal/spatial length-scales, sources of uncertainty,
15 observation operator...).

### 3.2 Data assimilation variables

#### 3.2.1 Observation variables and their errors

The observation vector, denoted $\mathbf{y}_k^o$ at the assimilation cycle $k$, is composed of the $n_y$ available observations at cycle $k$:

$$\mathbf{y}_k^o = \begin{bmatrix} y_{k,1}^o & y_{k,2}^o & \cdots & y_{k,n_y}^o \end{bmatrix} \tag{5}$$

20 where $y_{k,j}^o$, $j = 1 \ldots n_y$, is the $j$-th observation among the $n_y$ at cycle $k$.

In the present study, the observed variables are water depths issued from a SWOT simulator. As in Biancamaria et al. (2011) and Pedinotti et al. (2014), this SWOT simulator replicates SWOT spatio-temporal coverage. At a given date, the simulator selects the ISBA-CTRIP cells contained (at least 50% of their area) in the SWOT ground tracks. Figure 2 shows some selected ISBA-CTRIP cells under the real swaths over the Amazon basin. The true run is used as a basis to get the true water depths
25 $\mathbf{y}_k^t$. Then, to generate the observation vector $\mathbf{y}_k^o$ from the extracted true water depths, each of them is randomly perturbed by adding a white noise characterized by a standard deviation $\sigma^o$ such that:

$$\forall j = 1 \ldots n_y, \ y_{k,j}^o = y_{k,j}^t + \epsilon_j^o, \ \epsilon_j^o \simeq \mathcal{N}(0, \sigma^o). \tag{6}$$

The observation error is the addition of the measurement error and the representativeness error. The first is associated to inherent instrumental errors when processes are observed and the second represents the error introduced when the observed

and simulated variables are not exactly the same (in nature or scale). Following the SWOT uncertainty requirements (Esteban Fernandez, 2017), SWOT-like water surface elevation measurements have a vertical accuracy of 10 cm (when averaged over a water area of 1 km$^2$). This uncertainty accounts for measurement errors due to the remotely-sensed acquisition such as instrumental thermal noise, speckle, troposphere and ionosphere effects. Moreover, we omit error correlations along the swath

5 so that observation errors follow a white noise model. Accounting for spatially-correlated observation errors is an active research area in the field of data assimilation that is beyond the scope of demonstrating the feasibility of assimilating SWOT-type data (Guillet et al., 2018). Finally, in the framework of OSSE, observed and simulated water depths have the same scale as the ISBA-CTRIP model is used to generate both. Therefore, in the following, we assume there is no representativeness error in the system. Ultimately, $\sigma^o$ is chosen equal to 10 cm.

10 ### 3.2.2 Control, observation space and their errors

The control vector is denoted by $\mathbf{x}_k \in \mathbb{R}^{n_x}$. It includes the $n_x$ uncertain variables to be estimated through the $k$-th data assimilation cycle. The choice of the control variables determines the observation operator $\mathcal{H}_k$:

$$\mathbf{y}_k = \mathcal{H}_k(\mathbf{x}_k), \tag{7}$$

where $\mathbf{y}_k$ are the simulated observables, i.e. the mapping of the control variables onto the observation space. They are then

15 compared to the measured observations $\mathbf{y}_k^o$ during the data assimilation experiment. This comparison is referred to as the innovation vector.

In the present study, the control vector is composed of the $n_x$ multiplying factors $N_{\mathrm{mult},i}$, $i = 1 \ldots n_x$, applied to correct the spatial distribution of the river Manning coefficient:

$$\mathbf{x}_k = \left[ N_{\mathrm{mult},1} \ldots N_{\mathrm{mult},n_x} \right]^T. \tag{8}$$

20 Here, $n_x = 9$ as each multiplying factor is applied to one of the hydro-geomorphological areas defined in Section 2.3 and illustrated in Figure 1b.

The observation operator $\mathcal{H}_k$ maps the control variables (Manning coefficients dimensionless multiplying factors) into the observables (river water depths in meters) as follows:

1. first, apply the ISBA-CTRIP model $\mathcal{M}_{[k-1,k]}$ over the assimilation window $[k-1,k]$ to determine the model states that

25     correspond to the Manning coefficients ($\mathbf{x}_k$);

2. then, turn the CTRIP surface water storage into equivalent water depths following Eq. 3 (we denote by $\mathcal{Z}_k$ the diagnostic operator turning the surface storage variable into the water depth variable);

3. finally, select the simulated water depths under the SWOT swath mask (we denote by $\mathcal{S}_k$ this operator).

Therefore, the observation operator is the composition of three operators:

30 $$\mathbf{y}_k = \left( \mathcal{S}_k \circ \mathcal{Z}_k \circ \mathcal{M}_{[k-1,k]} \right)(\mathbf{x}_k) = \mathcal{H}_k(\mathbf{x}_k). \tag{9}$$

Such non-linear observation operator $\mathcal{H}_k$ is difficult to formulate explicitly. That is why we use an EnKF algorithm to estimate the Kalman gain in a statistical way.

### 3.3 The EnKF general formulation

In the EnKF framework, the model $\mathcal{M}_{[k-1,k]}$ and observation $\mathcal{H}_k$ operators are not linear. The main assumption for the EnKF

5   is to use stochastic ensembles to represent first- and second-order moments (namely the means and the covariances) of the control variable errors (Evensen, 1994, 2003). Indeed, it is assumed that the distribution of the ensemble is similar to that of the error of the control vector and it is also assumed that the Probability Density Function (PDF) of the error is gaussian, thus well described by its first and second moments. Therefore, the background control variables $\mathbf{x}_k^b$ (the first guess) are represented by an ensemble of $n_e$ members:

10 $$\mathbf{X}_{e,k}^b = \begin{bmatrix} \mathbf{x}_k^{b,[1]} & \mathbf{x}_k^{b,[2]} & \dots & \mathbf{x}_k^{b,[n_e]} \end{bmatrix}, \tag{10}$$

To avoid ensemble collapse, a supplementary noise is added to the observation vector $\mathbf{y}_k^o$ (Burgers et al., 1998). An observation ensemble is generated:

$$\mathbf{Y}_{e,k}^o = \begin{bmatrix} \mathbf{y}_k^{o,[1]} & \mathbf{y}_k^{o,[2]} & \dots & \mathbf{y}_k^{o,[n_e]} \end{bmatrix}. \tag{11}$$

Note that there exists alternatives to the observation randomization chosen here. However, for the present study, we choose to

15   use a full stochastic filter.

Finally, the EnKF analysis step is applied to each member of the ensemble such that

$$\forall\, l = 1 \dots n_e,\ \mathbf{x}_k^{a,[l]} = \mathbf{x}_k^{b,[l]} + \mathbf{K}_{e,k} \left( \mathbf{y}_k^{o,[l]} - \mathcal{H}_k(\mathbf{x}_k^{b,[l]}) \right), \tag{12}$$

where $\mathbf{K}_{e,k}$ is the the Kalman gain. It is built from the control and observation error covariance matrices $\mathbf{P}$ and $\mathbf{R}$ and the linearized observation operator $\mathbf{H}$ such that (see Appendix A for more details):

20 $$\mathbf{K}_{e,k} = [\mathbf{PH}^T]_{e,k} \left( [\mathbf{HPH}^T]_{e,k} + \mathbf{R}_k \right)^{-1}. \tag{13}$$

Figure 3 summarizes the general OSSE framework used for the present study. The figure reads from top to bottom and from left to right. An assimilation cycle $[k-1,\ k]$ includes a forecast step where is integrated an ensemble of ISBA-CTRIP simulations, each member having a different spatially-distributed Manning coefficient; an analysis step where the ensemble of Manning coefficients is corrected using synthetic observations through the Kalman filter update in Eq. 12; and a cycling step

25   where the ISBA-CTRIP model is re-run with these analysis estimates to obtain updated model states.

### 3.4 SWOT-based data assimilation special feature

#### 3.4.1 Choice of the assimilation window

We use a 21-day assimilation window corresponding to SWOT orbit revisit period. Therefore, during one assimilation window, every pixel under the observation mask is observed at least once. However, its implies that new observations are available

at times different from the update time. Such case has already been addressed in several studies. The Ensemble Kalman Smoother (EnKS) for example, introduced by Evensen and Leeuwen (2000), is a direct extension of the EnKF. It consists in, when a new observation is available, generating an update of the control variables taking into consideration the present and all past observations. The EnKS is actually a sequential version of the Ensemble Smoother (Leeuwen and Evensen, 1996).

5 The latter takes into consideration all past and future observations but turned out to be less effective than the EnKF and the EnKS (Evensen, 1997; Evensen and Leeuwen, 2000). Alternatively, Hunt et al. (2004) developed the 4D-EnKF (4D as in the 4D-VAR variational assimilation methods ; Talagrand and Courtier, 1987), which also assimilates observations available at different time-steps. In the 4D-EnKF, all model observations are expressed as a linear combination of the model observations at analysis time and the problem is transformed into a classical EnKF problem. Similarly, Hunt et al. (2007) also presented an

10 asynchronous version of the Local Ensemble Transform Kalman Filter (Bishop et al., 2001; Ott et al., 2004). In the framework of the present study, we apply an Asynchronous Ensemble Kalman Filter (AEnKF) as described by Sakov et al. (2010) and Rakovec et al. (2015). The principle is to increase the dimension of the state in order to consider observations at past and analysis times. This increases the dimension of the matrices which contain covariances between observations available at different times. To our knowledge, the AEnKF has not been used for parameter estimation, as Sakov et al. (2010) and Rakovec

15 et al. (2015) described the method for state estimation experiments.

### 3.4.2 The Asynchronous EnKF

To start with, $k$ represents the assimilation cycle index but it needs to be distinguished from the day index (within the assimilation cycle) which is the time unit for the observations. Then, we will denote by $k(i)$, $i = 1 \ldots 21$, the $i$-th day in the current assimilation cycle.

20 At the $i$-th day of the $k$-th assimilation cycle, the $n_{y,k(i)}$ observations are gathered in the vector $\mathbf{y}^o_{k(i)}$. Then, the overall observation vector at cycle $k$, $\mathbf{y}^o_k$, concatenates the 21 daily observation vectors $\mathbf{y}^o_{k(i)}$ such as:

$$\mathbf{y}^o_k = \begin{bmatrix} \mathbf{y}^{o,T}_{k(1)} & \cdots & \mathbf{y}^{o,T}_{k(21)} \end{bmatrix}^T \in \mathbb{R}^{n_{y,k}}, \; n_y = \sum_{i=1}^{21} n_{y,k(i)}. \tag{14}$$

Similarly to the observation vector, the overall observation operator at the $k$-th cycle, $\mathcal{H}_k$, is the concatenation of the daily observation operators $\mathcal{H}_{k(i)}$, defined from Eq. 9, but by considering the operator $\mathcal{M}$ integrating the model between $k(0)$

25 $(=(k-1)(21))$ and $k(i)$ as well as the diagnostic and selection operators a time step $k(i)$, $\mathcal{Z}_{k(i)}$ et $\mathcal{S}_{k(i)}$.

The observation error covariance matrix $\mathbf{R}_k$ is the concatenation of the daily observation error covariance matrices:

$$\mathbf{R}_k = \begin{pmatrix} \mathbf{R}_{k(1)} & & & \\ & \mathbf{R}_{k(2)} & 0 & \\ & 0 & \ddots & \\ & & & \mathbf{R}_{k(21)} \end{pmatrix} \text{ with } \mathbf{R}_{k(i)} = (\sigma^o)^2 \mathbf{I}_{n_{y,k(i)}}, \tag{15}$$

where $\mathbf{I}_{n_{y,k(i)}}$ is the identity matrix of size $n_{y,k(i)} \times n_{y,k(i)}$. It turns out that:

$$\mathbf{R}_k = (\sigma^o)^2 \mathbf{I}_{n_y}. \tag{16}$$

Following the same equations as the EnKF, the AEnKF generates, for each member $l = 1 \ldots n_e$ of the control ensemble, an analysis control vector $\mathbf{x}_k^{a,[l]}$.

### 3.4.3 Generation of the ensemble

The ensemble of background control vectors $\mathbf{X}_{e,k}^b$, of size $n_x \times n_e$, is generated such as $\mathbf{x}_k^{b,[l]}$, $l = 1 \ldots n_e$, follows a gaussian

5    law of mean $\overline{\mathbf{x}_k^b}$ and covariance matrix $\mathbf{P}_{e,k}^b$. For the first assimilation cycle, the control variables mean value $\overline{\mathbf{x}_1^b}$ is arbitrary chosen as the openloop run input parameter (the openloop or free run is the model run without any assimilation step) and the background error covariance matrix $\mathbf{P}_{e,1}^b$ is a diagonal matrix defined as

$$\mathbf{P}_{e,1}^b = \left( (\sigma^b)^2 \mathbb{I}_{n_x} \right)$$

with $\mathbb{I}_{n_x}$ the identity matrix of size $n_x \times n_x$ and $\sigma^b$ the vector that gathers the initial control variable error standard deviation.

10    Once the analysis ensemble $\mathbf{X}_{e,k}^a$ is determined, the next step is to propagate the correction in time. In a standalone PE framework, it is necessary to re-run the ensemble model runs during the current assimilation window with the analysis parameters as inputs. Then, the contribution of the updated parameters is propagated through the model, up to the end of the current assimilation window and put into the model initial condition for the next assimilation cycle.

For the next assimilation cycles, the background mean estimate is set equal to the analysis mean estimate from the previous

15    cycle:

$$\overline{\mathbf{x}_k^b} = \overline{\mathbf{x}_{k-1}^a}.$$

There are different ways of defining $\mathbf{P}_{e,k}^b$. One could choose to stochastically estimate $\mathbf{P}_{e,k-1}^a$ from the analysis ensemble at the previous cycle and use it as $\mathbf{P}_{e,k}^b$. Contrary to state estimation experiment where the analysis error covariance matrix is propagated in time using the model along with the control variables, parameter estimation experiment directly uses it as the

20    background error covariance matrix since there is no dynamical model for the Manning coefficient. The issue with this approach is that the analysis ensemble variance can be strongly reduced and give too small ensemble spread to have efficient AEnKF update in time. To ensure that enough uncertainty is maintained in the ensemble, one can maintain the initial background error covariance matrix through all cycles or impose a minimal value for the variance elements (see Section 5.4).

The background error cross-covariance matrix $[\mathbf{PH}^T]_{e,k}$ and covariances matrix $[\mathbf{HPH}^T]_{e,k}$ are directly built from the

25    definition suggested by Evensen (2004), Moradkhani et al. (2005) and Durand et al. (2008), see Appendix A for more details. The matrices are of size $n_x \times n_{y,k}$ and $n_{y,k} \times n_{y,k}$ respectively. The elements in the error cross-covariance matrices directly result from the characterization of the background ensemble, namely the parameter uncertainties accounted for to generate the control matrix $\mathbf{X}_{e,k}^b$ and $\mathcal{H}(\mathbf{X}_{e,k}^b)$.

## 4 Assimilation strategy

In the incoming experiments, the true control variables $\mathbf{x}^t$ are:

$$\mathbf{x}^t = \begin{bmatrix} 1.65 & 0.85 & 0.85 & 0.95 & 0.90 & 0.95 & 0.90 & 1.30 & 1.40 \end{bmatrix} \tag{17}$$

and the background for the first assimilation cycle $\overline{\mathbf{x}_1^b}$ are:

$$\overline{\mathbf{x}_1^b} = \begin{bmatrix} 1.50 & 0.50 & 0.50 & 0.50 & 0.50 & 0.50 & 0.50 & 1.50 & 1.50 \end{bmatrix}. \tag{18}$$

Basically, we increase the Manning value in mountainous zones (zones 1 in the Andes and zones 8 and 9 over the shields) and lower the Manning value over the other zones with the lowest values (in zones 2 and 3) corresponding to the main stem. Both true and background values were chosen accordingly.

### 4.1 Sensitivity tests

10   During one EnKF assimilation cycle, the analysis potentially depends on the following parameters: model spin up, time period (high/low flow), size of the ensemble, control error. Note that the observation error also have an impact on the analysis but its value is already fixed for all subsequent experiments (see Section 5).

A first set of experiments (either model runs or data assimilation runs) will serve as sensitivity tests for the data assimilation platform with respect to the above features. During these sensitivity tests, the different features are tested individually. Table 1

15   details the range of variations for each tested feature.

### 4.2 Assimilation tests

Following the sensitivity tests, a set of three data assimilation experiments will be run and is presented in Table 2. The data assimilation experiments are divided in two categories: the first one uses water depths as observations and the second one considers water depth anomalies. All experiments are run over a year, corresponding to 17 assimilation cycles of 21 days.

20   The first experiment, denoted as PE1, is configured from the aforementionned sensitivity test outcome. The parameters defining the experiment (spinup, starting date, ensemble size, control error) will be those giving the best results in the sensitivity tests in Table 2. Also, the reference level between the observed and simulated water depths is the same. In other words, there is no bias in the observation. This first idealized experiment serves as proof-of-concept.

The next step is to go towards more realistic experiments by including new sources of uncertainties in the data assimilation

25   system and see how to address them. In this context, two additional experiments denoted as PE2 and PE3 will be carried out. As an example of new uncertainties, SWOT will actually observe water elevations (water surface elevation as referenced to a geoid or an ellispsoid) while CTRIP produces water depths (water surface elevation as referenced to the bottom of the river bed). To perform data assimilation, one needs to convert CTRIP water depths ($h_S^{\mathrm{CTRIP}}$) into CTRIP water elevations ($H_{\mathrm{alti}}^{\mathrm{CTRIP}}$) or inversely for SWOT. It is highly plausible that this operation induces a bias between the modeled and observed water elevations.

30   A simplified example of such situation is illustrated in Figure 4. In this case, SWOT catches the right water elevation dynamic

(as $h_S^{\text{SWOT}}$ and $h_S^{\text{CTRIP}}$ are equal) but the direct assimilation of SWOT water elevation $H_{\text{alti}}^{\text{SWOT}}$ will induce a bias as the elevations of the river bed ($H_{\text{bed}}^{\text{SWOT}}$ and $H_{\text{bed}}^{\text{CTRIP}}$) are different between CTRIP and SWOT.

A solution to handle this issue is to assimilate water depth anomalies instead of water depths. Therefore, the next data assimilation experiments, denoted as PE2 and PE3, will test the feasability of assimilating anomalies. In these experiments,

5   the water depth anomalies are generated by substracting a time-averaged reference water depth to the current water depth. For all runs (true, openloop or analysis), this time-averaged reference water depth is computed as the mean (true, openloop or analysis) water depth over the year before the start of the assimilation window. It is therefore different for each member of the ensemble. First, in experiment PE2, there will still be no bias between the observed and simulated river bed slopes to see how the assimilation of anomalies performs. Finally, the last experiment PE3, which introduces a constant relative bias between

10  CTRIP and SWOT, will be carried out.

## 5   Assimilation sensitivity tests

### 5.1   Model spinup sensitivity tests

The objective of the spinup sensitivity tests is to evaluate the minimum spinup period required by the model before applying data assimilation. For this purpose, the model is run several times over two years, from December 19th, 2006 to December

15  22nd, 2008, which corresponds to 35 windows of 21 days (735 days).

A first simulation is run using the true Manning spatial distribution (see Eq. 17) over the two-year time period. Then, we run 18 additional simulations over the same period with a varying length of the spinup period (see Table 1). Initially, the simulation setup corresponds to the openloop configuration with the openloop Manning spatial distribution (see Eq. 18). At a given time during the first year, the Manning spatial distribution is instantaneously changed to the true distribution (see Eq. 17) and the

20  model is run until the end of the two years with the true Manning spatial distribution. Table 3 summarizes for each run, the date when the Manning coefficients are changed. The spinup period (expressed as a number of windows of 21 days) corresponds to the period between when the Manning distribution is changed and the start of the second year, i.e. January 1st, 2008.

To evaluate the spinup impact, the relative difference between the reference run and the test runs is evaluated over the second year of simulation (from January 1st to December 22nd, 2008) and averaged over every window of 21 days. Figure 5 presents

25  the results for the spinup sensitivity test. Each test run (on the x-axis) is identified by its corresponding spinup period length (expressed as the number of windows of 21 days, see Table 3). Then, we count (on the y-axis) the number of 21-day windows during which the relative error between the test run and the reference run is higher than a given threshold. We assume that the spinup period is long enough when this number is equal to 0. This number is evaluated from the basin-averaged relative difference and from the relative difference at the downstream station of Obidos, both in terms of water depth and discharge.

30  Note that in Figure 5, when the number of spinup windows of 21 days is equal to 4 on the x-axis, the change from the openloop Manning distribution to the true one is imposed on October 9th, 2007. Similarly, when this number is equal to 10, the change is imposed on June 5th, 2007. Note also that two thresholds are considered, 0.01 and 0.001. Basin-averaged results are not

sensitive to this threshold. There are some differences at Obidos; however, we retain the upper case to evaluate the required model spinup period.

From all the results we conclude that a minimum spinup period of 4 windows of 21 cycles, i.e. 84 days, is required. In the following sensitivity tests, the model runs start on October 9th, 2007, to be consistent with these results.

## 5.2 Data assimilation starting date sensitivity tests

To evaluate the impact of the starting date, a set of 17 one-cycle-long data assimilation experiments is carried out over the second running year. All experiments have the same general configuration except for the initial date starting from January 1st, 2008 and shifted by 21 days until December 22nd, 2008. This means that the last experiment starts on December 2nd, 2008. The performance of each experiment is evaluated by simply evaluating the spatial average difference between the analysis and the true Manning coefficients. Results presented in Figure 6a-b indicate that there is no significant differences between the data assimilation experiments (for all 17 experiments, the error of the updated Manning coefficients with respect to the true value of the coefficients is below 5 %).

Note that the results in Figure 6a-b show a light increase of the statistics for the experiment starting at the end of the year, presently starting from September 9th to December 2nd, 2008. This period corresponds to the low-flow season in the Amazon hydrological cycle. Back to the sensitivity analysis results (Emery et al., 2016), the water depths showed a very low sensitivity to the Manning coefficient during the low flow season. As a consequence for data assimilation, the EnKF is less performant in low flow season to correct the Manning coefficient. Therefore, the analysis relative error (in Figure 6a) and the analysis ensemble dispersion (in Figure 6b) is higher in low flow season.

Thus, for all next sensitivity tests, we only consider one-assimilation-cycle experiments starting on January 1st, 2008.

## 5.3 Ensemble size sensitivity tests

The next sensitivity test is dedicated to the ensemble size $n_e$, which is a critical parameter of any EnKF algorithm. This parameter has to be high enough to accurately estimate the Kalman gain matrix but low enough to limit the computational cost (the higher $n_e$, the more model runs are required over each data assimilation window to obtain the analysis estimate of the Manning coefficients).

We consider different ensemble sizes through a one-assimilation-cycle experiment, $n_e$ varies between 10 and 200. Figure 6c compares the analysis Manning coefficient relative error for each ensemble size $n_e$ as in Figure 6a. Results show that the analysis relative error decreases when the ensemble size $n_e$ increases. For an ensemble size $n_e$ equal to 20, the analysis error is below 5 %. Also, for an ensemble size $n_e$ higher than 50, the analysis relative error has converged to a constant value while the analysis ensemble dispersion showed in Figure 6d stabilises.

These results indicate the ensemble size for future data assimilation experiments should be at least equal to 20; we consider $n_e = 25$ in the present study to limit computational time.

### 5.4 Model error standard deviation sensitivity tests

In this work, we only consider parameter estimation, implying that the background error covariance matrix is associated with the parameter space. We assume that the errors in the Manning coefficients are independent so that the background error covariance matrix is initially specified as a diagonal matrix, where all diagonal elements correspond to the error variances in

5    the spatially- varying Manning coefficients and are equal to the same variance $(\sigma^b)^2$, where $\sigma^b$ is the background error standard deviation. Similarly to previous sensitivity tests, we study here the sensitivity of the data assimilation results to the value of $\sigma^b$ through a one-assimilation-cycle experiment. Figure 6c shows, in logarithmic-scale on the x-axis, the relative error of the updated Manning coefficient with respect to the true coefficient. The analysis error curve shows a decreasing behavior until $\sigma^b$ is on the order of 0.4, and then increases again.

10    Note that the actual Manning coefficient error before data assimilation is equal to 0.33 (see the blue curve in Figure 6c showing the openloop Manning coefficient error). Consistently, the best data assimilation results are obtained when $\sigma^b$ provides a good approximation of the real error standard deviation. Note also that when $\sigma^b$ becomes too small, data assimilation is less effective. The EnKF algorithm is known to be under-dispersive. Therefore, for future data assimilation experiments, when updating the error covariance matrix from one cycle to another, we will need to make sure that the ensemble dispersion is high

15    enough to cover possible model behavior over the forecast time window by imposing a minimum value for the error variance. Given the sensitivity test results, the minimum value for $\sigma^b$ is set to 0.005. Thus, in the following data assimilation experiments, we use the analysis error covariance matrix as the background error covariance matrix for the next assimilation cycle, while applying the minimum threshold value on the matrix diagonal terms.

## 6 Data assimilation results

20    We present now the results from the data assimilation experiments presented in Table 2 and in Section 4.4.2. Recall that these experiments aim at correcting the spatially-varying Manning coefficient in the nine zones covering the Amazon basin.

### 6.1 Assimilation of water depths (PE1)

Figure 7 gives, for each zone, the time evolution of the mean analysis control variable (red) with its dispersion (even though it is very narrow) compared to the truth (black) and the first guess (blue). Similarly, Figure 8 shows, for each zone, the time

25    evolution of the analysis water depth (red) compared to the truth (black) and the openloop (blue). To generate one plot per zone, we use, for each time step, the ensemble of water depths over all cells in the zone and estimate the median value, the first decile and the ninth decile.

     In general, the PE1 experiment gives very good results as the analysis mean for each zone retrieves the true value with a very low dispersion. However, the data assimilation algorithm features spatially-dependent behavior, see Figure 7):

30      - First, the control variable for the zones 2, 3, 4 and 5 converges instantaneously (in only one assimilation cycle) toward the true values and remains at these true values for all following cycles.

- A similar behavior can be observed for zones 6, 7 and 8 from the first cycle to around the ninth cycle. For the remaining cycles, we notice an increase of the mean analysis estimate, along with the ensemble dispersion, until around the thirteenth cycle and after, a decrease back to the true value.

- For the boundary zones, zones 1 and 9, the analysis estimates are closer to the truth than the first guess but there is no
5      clear convergence toward the true values.

Those observations can be explained with the global sensitivity analysis results for water depths in Emery et al. (2016) and using Figure 8:

- First, zones 1, 2 and 3 correspond to the river main stem, while zones 4, 5 and 9 correspond to the main left-bank tributaries, namely the Caquetá/Japurá river (zone 4) and the Negro river (zone 5). In these zones, as the Manning
10      coefficient is directly corrected in the first assimilation cycle, the analysis water depths (red) overlap the true water depth (black). Furthermore, Figure 8 for these zones shows that the openloop (blue) and true (black) water depths have a very similar variability in time but are different by a constant bias. The global sensitivity analysis results in these zones showed a constant first-order sensitivity in time to the Manning coefficient all year long. This first-order sensitivity means that the contribution of the Manning coefficient to the water depth is linear. Therefore, correcting the Manning coefficient in
15      these zone equates to correcting the bias between the openloop and the true water depths.

- Subsequently, zones 6, 7 and 8 correspond to right-bank tributaries, namely the Juruá and Purus rivers (zone 6), the Madeira river (zone 7) and the Tapajós and Xingu rivers (zone 8). These right-bank tributary zones are characterized by a strong seasonal cycle (see Figure 8, zones 6-8). Then, by comparing the corresponding plots in Figures 7 and 8, we notice that the period when the analysis control variable spreads from the truth corresponds to the low flow season
20      in these zones. According to the global sensitivity analysis results, water depths in these zones are not sensitive to the Manning coefficient in low flow conditions. Meanwhile, the EnKF still sees a positive discrepancy between the model and the observations (i.e. the observations are higher than the model predictions), as seen in the time evolution per zone of the innovation in Figure A1). Therefore, in order to increase the simulated water depth, the EnKF corrects the Manning coefficient so that its value gets higher (a higher Manning coefficient means a slower flow velocity and then a
25      higher simulated water depth). However, the water being insensitive to the Manning coefficient during this period, the correction is not transferred to the simulated water depth and the Manning coefficient value keeps being increased during the low flow season. Finally, once the low flow season ends, the analysis Manning coefficient converges back to the truth (see the last assimilation cycles).

## 6.2 Assimilation of water anomalies (PE2 and PE3)

30 The assimilation of anomalies has been tested over two experiments denoted PE2 and PE3 (see Table 2). Note that the observation error standard deviation $\sigma^o$ remains equal to 10 cm as, with these experiments, we only aim at testing the feasibility of assimilating water depth anomalies. In the PE2 experiment, there is no difference of bathymetry elevation between the DEM

used for the simulated water anomalies and the DEM used for the observed water anomalies while two different bathymetries are used in the PE3 experiment. Figure 9 gives, for each zone, the time evolution of the mean analysis control variable for PE2 (orange) and PE3 (purple) with their dispersion compared to the truth (black) and the first guess (blue).

The general configuration of the experiments PE1 and PE2 is the same. The only difference between the two experiments
5   is the nature of the observations: water depths for PE1 and water anomalies for PE2. Like experiment PE1, experiment PE2 (the orange line in Figure 9) gives very good results. All control variables converge toward the true values more or less rapidly. The control variable for the zones 4 to 8 instantaneously (in only one assimilation cycle) converges toward the true value while the convergence is slower for the remaining zones as around five assimilation cycles are needed to retrieve the true value. This slower convergence for these zones can be explained by the fact that the magnitude of the observed water anomalies is generally
10  smaller, compared to the water depths assimilated in PE1. Then, the ratio between the observation error and the observations themself is also smaller, resulting in a smaller EnKF gain. Therefore, the control variable correcting increment is smaller for the anomalies than for the water depth and more cycles are needed to converge.

Now, as for the PE3 experiment results - the purple line in Figure 9 - the assimilation still gives good results but not as good as the previous experiments. The control variables still instantaneously converge toward the truth in the zones 4, 5 and
15  6 but, for the other zones, the control variables get closer to the truth without really converging (zones 2 and 3) or sometimes temporarily deviate from the truth during the experiment (zones 1, 7, 8 and 9). Still, despite the control variables not clearly converge toward the truth, the simulated water depths using the analysis control variables, presented in Figure 10, are shown to be really close to the true water depths anyway, confirming the general good performance of the data assimilation procedure.

Comparing the control variables and water depth time variations, it appears that the control variables are deviating from the
20  truth mainly when the water depths are decreasing, in between the high flow and low flow seasons. During this period, the model goes from a state where floods occur to a state where there is no flood, particularly in the zones 2-3 and 7-8 with a clear seasonal cycle. On the other hand, no flood event was spotted in zones 4, 5 and 6 where the best results were obtained. In ISBA-CTRIP, the activation/deactivation of the flooding scheme is triggered by the simulated water depth exceeding/getting lower than the river bankful depth. Yet, in the experiment PE3, this river bankful depth is different between the model and
25  the observation because we artificially inserted a bias between the simulated and observed water depths. More specifically, the river bankful depth is lower in the model than in the observations. Therefore, the control variables deviating from the true value when the water depth is decreasing are indicative of the simulated water depths presenting floods while there is no flood in the observations. The activation of the flood scheme changes the dynamics of the water depth in the river. As part of the water in the river is spilled into the floodplains, water level variations in the river are slower. Then, the flooded model needs a stronger
30  variations of the Manning coefficient to catch the non-flooded observed water level. Ultimately, the stronger variations of the estimated Manning coefficient allow to retrieve the true water depths.

## 7 Discussions

In this study, we introduce the assimilation of water surface anomalies in order to handle a potential bias between the simulated and observed water depths. This bias originates from a discrepancy between the elevation of the river bed in the model and in the observations with respect to a reference surface such as a geoid or an ellipsoid (see Figure 4). Under the assumption that

5   the water variations are the same between the model and the observations, the use of anomalies as observed variables should prevent this bias from affecting the results. However, in this study, we did not have access to water surface elevations referenced to a geoid/ellipsoid as we led OSSE and we used the ISBA-CTRIP mode to create the observations. Therefore, the bias was artificially introduced by perturbing the model bankful depth. Thus, we actually introduced another type of bias in the system. Indeed, in ISBA-CTRIP, the river bankful depth controls when the model floods, which has a direct impact on the water depth

10   dynamics. Therefore, the bias that we introduced is linked to a different water elevations dynamics when either the observed variables flood and the model variables do not (and inversely). Furthermore, the experiment PE3 illustrated the effect of this bias on the variations of Manning coefficients. Instead of being maintained at the true value, their value slightly vary around the true values to account for the difference in dynamics between the model and the observations. In future work, in order to fully assess the assumption that the anomalies can prevent a bias due to the reference surface, we actually need to introduce

15   the elevation of the river bed into the data assimilation system.

Following these remarks, we emphasize that the DEM and the bathymetry used for the model are critical parameters for assimilation. As observed in the PE3 experiment, during an assimilation experiment, the error introduced by a high discrepancy between the model DEM/bathymetry and the observations/reality DEM/bathymetry is transferred to the control variables (here the Manning coefficients) as these variables are considered as the most uncertain. If this uncertainty were to get higher, we

20   could expect higher divergence of the Manning coefficients from the true values and even get non-physical/non-realistic values. Therefore, it is essential to limit this bias and its impact on the assimilation. Noting this, there may be an additional advantage in assimilating water anomalies instead of the direct water depths. Comparing the Kalman gain between the PE1 experiment (that assimilated direct water depths) and the PE2/PE3 experiments (that assimilated water anomalies), the gain magnitude for the water anomalies is lower than the water depth gain magnitude. This is to be expected as the Kalman gain is stochastically

25   estimated from an ensemble of model runs and the magnitude of the simulated water anomalies is lower than the simulated water depth magnitude. The consequence of this lower gain is the correction applied to the control variable is also lower. If the convergence toward the true value takes more than one assimilation cycle, the divergence from it in the presence of bias is also diminished.

Moreover, the Manning coefficient distribution is set to be constant in time. For each grid cell, one value of the Manning

30   coefficient is used for the entire simulation. However, in reality, it is commonly accepted that this parameter should vary in time, depending on the seasonal cycle or also some exceptional hydrological event. The results showed that the data assimilation is able to converge quite quickly towards the true value. For example, for the left-bank tributaries zones, namely zones 4 and 5, in every experiment, the associated control variable converges toward the true value in only one assimilation cycle. Then, in

a real-case experiment, we could expect to retrieve the temporal variations of the Manning coefficient from one assimilation cycle to another.

The good performances of the assimilation platform are mainly related to the fact that, in the ISBA-CTRIP model, the water depth diagnostic variables are sensitive to the Manning coefficient (Emery et al., 2016). Thus, when the simulated water depth

5   is not that sensitive to the Manning coefficient, for example in the right-bank tributary zones during the low flow season, the data assimilation performances slightly degrade. These results are specific to the ISBA-CTRIP model. To apply the same method to another model and even another region, one need to first study the sensitivity of the (other) model to the (other) study region.

The results presented here are preliminary investigations to the assimilation of the SWOT water surface elevations product

10  into a large scale hydrological model. The real SWOT data will have a finer resolution than the synthetical SWOT data currently used. Still, the coarser resolution observations are found to provide information to constraint the model and improve the value of the spatially-varying Manning coefficients. Then, when moving to real-data assimilation experiments, we can consider averaging the fine-scale SWOT product over a coarse grid cell corresponding to an ISBA-CTRIP cell so that the resolution of the observations and the model matches.

## 8   Conclusions

This study presents a series of OSSE that assimilates SWOT-like synthetic observations of water elevations into the large-scale hydrological model ISBA-CTRIP in order to correct the spatially-distributed Manning coefficient. The study is applied over the Amazon river basin. Prior to the actual data assimilation experiments, a series of sensitivity tests was conducted to study the sensitivity of the data assimilation performance to the different features of the EnKF, in particular the size of the

20  ensemble. Then, three full-year data assimilation experiments were run based on the outcomes of the sensitivity tests. For all three experiments, the assimilation was able to track back the true value of the Manning coefficient distribution.

The sensitivity tests successively studied the sensitivity of the data assimilation platform to model spinup period, the experiment starting date through the hydrogical year, the size of the ensemble for the EnKF and the initial control variable standard deviation. These tests showed first that a spin up of four windows of 21 days are enough to go through the transitional period

25  due to a sudden change in the Manning coefficient distribution in the model. Then, the second sensitivity test demonstrated that the data assimilation performance is not clearly sensitive to the period of the hydrological year when the experiment is done. The next sensitivity test informed us that an ensemble of 25 members was enough to obtain good EnKF performances. Finally, the last sensitivity test studied the effect of the control variable error standard deviation and the best performances were obtained for prior standard deviation between 0.05 and 0.75, which corresponds to the order of magnitude of the actual error

30  between the true and openloop control variables.

Using these results, we run three data assimilation experiments over approximately one year (the year 2008). The first experiment (PE1) assimilated direct pseudo-observations of water depths. Results showed the capability of the data assimilation algorithm to converge very quickly toward the true value, generally in only one assimilation cycle. Still, during the low flow

season, the assimilation was less effective in the zones with a clear seasonal cycle. This was explained by the fact that during this period, the water depths are less sensitive to the Manning coefficient.

The two other experiments (PE2 and PE3) introduced and tested the assimilation of water surface anomalies. The anomalies were obtained by substracting a yearly-averaged water depths to the current water depth in both the model and the observations.
5  The first water anomalies assimilation experiment (PE2) gave very good results with also all the control variables converging toward their associated true values. However, the convergence was slightly slower than during the assimilation of the water depth (between 1 and 5 assimilation cycles). This is explained by a lower Kalman gain when updating the Manning coefficient.

The last experiment also assimilated water anomalies (PE3). But, for this particular experiment, a bias was artificially introduced in the river bathymetry. For this experiment, the assimilation was still able to get closer to the true value but, for the
10  some zones like the mainstream zones, there was no convergence as the control variables kept varying around the true value. This phenomenon was explained by the detection of floods in the model but not in the observations. Still, the statistics of the Manning coefficient distribution and the simulated water depths after assimilation remain improved compared to the openloop simulations. Ultimately, these two experiments demonstrated the feasibility of assimilating water surface anomalies to correct the Manning coefficient.

15  These experiments offer several perspectives. They mainly consist in going towards more realistic data assimilation experiments that take into account more source of uncertainties between the model and the observations (such as correlated observation errors). To test the limit of the platform performances regarding the DEM/bathymetry bias issue, one can use simulated water surface elevations referenced to a geoid instead of water depth from the model or even assimilate water depth from another model where the bathymetry is different. Along with observations of water surface elevations, SWOT will also
20  provide two-dimensional maps of river width and surface slope. One can also study the possibility of assimilating such product to correct the corresponding parameters in ISBA-CTRIP such as the model river width or maybe constrain other parameters such as the bankful depth that controls the model flooding scheme.

*Code and data availability.* The CTRIP code is open source and is available as a part of the surface modelling platform called SURFEX, which can be downloaded at http://www.cnrm-game-meteo.fr/surfex/. SURFEX is updated approximately every 3 to 6 months and the
25  CTRIP version presented in this paper is from SURFEX version 7.3. If more frequent updates are needed, please follow the procedure to obtain a SVN or Git account in order to access real-time modifications of the code (see the instructions at the previous link). The ISBA-CTRIP model is coupled to the DA codes via the OpenPalm coupler available at http://www.cerfacs.fr/globc/PALM_WEB/. To get the DA routines coupled to ISBA-CTRIP with OpenPalm, please directly contact C. Emery (charlotte.emery@jpl.nasa.gov) or S. Biancamaria (sylvain.biancamaria@legos.obs-mip.fr). To obtain the GSWP3 forcings, please refer to the following url: http://search.diasjp.net/en/dataset/
30  GSWP3_EXP1_Forcing (https://doi.org/10.20783/DIAS.501).

## Appendix A: Definition of error covariance matrices

The background error cross-covariance matrices $[\mathbf{PH}^T]_{e,k}$ and $[\mathbf{HPH}^T]_{e,k}$ are defined based on Evensen (2004); Moradkhani et al. (2005); Durand et al. (2008) such that:

$$[\mathbf{PH}^T]_{e,k} = (n_e - 1)^{-1} \left( \mathbf{X}^b_{e,k} - \overline{\mathbf{X}^b_{\bullet,k}}.\mathbf{1}^T_{n_e} \right) \left( \mathcal{H}(\mathbf{X}^b_{e,k}) - \overline{\mathcal{H}(\mathbf{X}^b_{\bullet,k})}.\mathbf{1}^T_{n_e} \right)^T, \tag{A1}$$

5  and

$$[\mathbf{HPH}^T]_{e,k} = (n_e - 1)^{-1} \left( \mathcal{H}(\mathbf{X}^b_{e,k}) - \overline{\mathcal{H}(\mathbf{X}^b_{\bullet,k})}.\mathbf{1}^T_{n_e} \right) \left( \mathcal{H}(\mathbf{X}^b_{e,k}) - \overline{\mathcal{H}(\mathbf{X}^b_{\bullet,k})}.\mathbf{1}^T_{n_e} \right)^T. \tag{A2}$$

In those definitions, $\mathbf{X}^b_{e,k}$ is the control matrix storing the $n_e$ control vectors $\mathbf{x}^{b,[l]}_k$, $l = 1 \ldots n_e$, from the background ensemble such that

$$\mathbf{X}^b_{e,k} = \left[ \mathbf{x}^{b,[1]}_k \ \ldots \ \mathbf{x}^{b,[N_e]}_k \right]$$

10  .

Next, $\mathcal{H}(\mathbf{X}^b_{e,k})$ represents the same control matrix but mapped into the observation space:

$$\mathcal{H}(\mathbf{X}^b_{e,k}) = \left[ \mathcal{H}(\mathbf{x}^{b,[1]}_k) \ \ldots \ \mathcal{H}(\mathbf{x}^{b,[n_e]}_k) \right].$$

Also, $\overline{\mathbf{X}^b_{\bullet,k}}$ and $\overline{\mathcal{H}(\mathbf{X}^b_{\bullet,k})}$ are the corresponding ensemble expectations such that

$$\overline{\mathbf{X}^b_{\bullet,k}} = \frac{1}{n_e} \sum_{l=1}^{n_e} \mathbf{x}^{b,[l]}_k \quad \overline{\mathcal{H}(\mathbf{X}^b_{\bullet,k})} = \frac{1}{n_e} \sum_{l=1}^{n_e} \mathcal{H}(\mathbf{x}^{b,[l]}_k).$$

15  These vectors dimension are $n_x$ and $n_{y,k}$ respectively. Finally, $\mathbf{1}_{n_e}$ is a vector of size $n_e$ containing only 1s.

## Appendix B: Assimilation results additional figures

*Author contributions.*  Charlotte M. Emery designed and carried out the experiments under the supervision of Sylvain Biancamaria and Aaron Boone, as part of her PhD project. Sylvain Biancamaria provided the SWOT-based observation mask used to generate the synthetic observations and Aaron Boone provided support on the use of the ISBA-CTRIP hydrologic model. Charlotte M. Emery prepared the manuscript

20  with contribution from all co-authors.

*Competing interests.*  The authors declare that they have no conflict of interest.

*Acknowledgements.*  This work was supported by the CNES, through a grant from Terre-Océan-Surfaces Continentales-Atmosphère (TOSCA) committee attributed to the project entitled "Towards an improved understanding of the global hydrological cycle using SWOT measurements". C. M. Emery received doctoral research support from CNES/région Midi-Pyrénées grant. C. M. Emery and C. H. David received

support from the Jet Propulsion Laboratory, California Institute of Technology, under a contract with NASA; including grants from the SWOT Science Team and the Terrestrial Hydrology Program.

# References

Beven, K. and Freer, J.: Equifinality, data assimilation, and uncertainty estimation in mechanistic modelling of complex environmental systems using GLUE methodology, Journal of Hydrology, 249, 11–29, https://doi.org/10.1016/S0022-1694(01)00421-8, 2001.

Beven, K. J.: Rainfall-Runoff modelling, chap. Chap 1: Down to basics: runoff processes and the modelling of processes, pp. 1–22, John Wiley and Sons, West Sussex, UK, 2012.

Biancamaria, S., Durant, M., Andreadis, K. M., Bates, P. D., Boone, A., Mognard, N. M., Rodriguez, E., Alsdorf, D. E., Lettenmaier, D. P., and Clark, E. A.: Assimilation of virtual wide swath altimetry to improve Arctic river modeling, Remote Sensing of Environment, 115, 373–381, https://doi.org/10.1016/j.rse.2010.09.008, 2011.

Bierkens, M. F. P.: Global hydrology 2015: State, trends, and directions, Water Resources Research, 51, 4923–4947, https://doi.org/10.1002/2015WR017173, 2015.

Birkett, C. M., Mertes, L. A. K., Dunne, T., Costa, M. H., and Jasinski, M. J.: Surface water dynamics in the Amazon basin: Application of satellite radar altimetry, Journal of Geophysical Research, 107, https://doi.org/10.1029/2001JD000609, 2002.

Bishop, C. H., Etherton, B. J., and Majumbar, S. J.: Adaptative sampling with the ensemble transform Kalman filter. Part I: Theoretical aspects, Monthly Weather Review, 129, 420–436, https://doi.org/10.1175/1520-0493(2001)129<0420:ASWTET>2.0.CO;2, 2001.

Boone, A., Calvet, J.-C., and Noilhan, J.: Inclusion of a Third Soil Layer in a Land Surface Scheme Using the Force-Restore Method, Journal of Hydrometeorology, 38, 1611–1630, https://doi.org/10.1175/1520-0450(1999)038<1611:IOATSL>2.0.CO;2, 1999.

Burgers, G., Leeuwen, P. J. V., and Evensen, G.: Analysis Scheme in the Ensemble Kalman Filter, Monthly Weather Review, 126, 1719–1724, https://doi.org/10.1175/1520-0493(1998)126<1719:ASITEK>2.0.CO;2, 1998.

Clark, M. P., Rupp, D. E., Woods, R. A., Zheng, X., Ibbitt, R. P., Slater, A. G., Schmidt, J., and Uddstrom, M. J.: Hydrological data assimilation with the ensemble Kalman filter: Use of streamflow observations to update states in a distributed hydrological model, Advances in Water Resources, 31, 1309–1324, https://doi.org/10.1016/j.advwatres.2008.06.005, 2008.

Cretaux, J.-F., Calmant, S., Romanoski, V., Shabunin, A., Lyard, F., Berge-Nguyen, M., Cazenave, A., Hernandez, F., and Perosanz, F.: An absolute calibration site for radar altimeters in the continental domain: Lake Issykkul in Central Asia, Journal Of Geodesy, 83, 723–735, https://doi.org/10.1007/s00190-008-0289-7, 2009.

Decharme, B., Alkama, R., Douville, H., Becker, M., and Cazenave, A.: Global Evaluation of the ISBA-TRIP Continental Hydrological System. Part II: Uncertainties in River Routing Simulation Related to Flow Velocity and Groundwater Storage, J. Hydrometeor., 11, 601–617, https://doi.org/10.1175/2010JHM1212.1, 2010.

Decharme, B., Alkama, R., Papa, F., Faroux, S., Douville, H., and Prigent, C.: Global off-line evaluation of the ISBA-TRIP flood model, Climate Dynamics, 38, 1389–1412, https://doi.org/10.1007/s00382-011-1054-9, 2012.

Decharme, B., C., D., Minvielle, M., J., C., J.-P., V., D., A. A. S.-M., R., S., S., S., and A., V.: Recent changes in the ISBA-CTRIP land surface system for use in CNRM-CM6 climate model and global off-line hydrological applications., Journal of Advances in Modeling Earth Systems, 11, https://doi.org/10.1029/2018MS001545, 2019.

Deng, C., Liu, P., Guo, S., Li, Z., and Wang, D.: Identification of hydrological model parameter variation using ensemble Kalman filter, Hydrology and Earth System Sciences, 20, 4949–4961, https://doi.org/10.5194/hess-20-4949-2016, 2016.

Doll, P., Douville, H., Güntner, A., Schmied, H. M., and Wada, Y.: Modelling Freshwater Resources at the Global Scale: Challenges and Propects, Surveys in Geophysics, 37, https://doi.org/10.1007/s10712-015-9343-1, 2015.

Durand, M., Andreadis, K., Alsdorf, D., Lettenmaier, D., Moller, D., and Wilson, M.: Estimation of bathymetric depth and slope from data assimilation of swath altimetry into a hydrodynamic model, Geophysical Research Letters, 35, https://doi.org/10.1029/2008GL034150, 2008.

Emery, C. M., Biancamaria, S., Boone, A., Garambois, P.-A., Ricci, S., Rochoux, M. C., and Decharme, B.: Temporal variance-based sensitivity analysis of the river routing component of the large scale hydrological model ISBA-TRIP: Application on the Amazon Basin, Journal of Hydrometeorology, 17, 3007–3027, https://doi.org/10.1175/JHM-D-16-0050.1, 2016.

Emery, C. M., Paris, A., Biancamaria, S., Boone, A., Calmant, S., Garambois, P.-A., and Silva, J. S. D.: Large scale hydrological model river storage and discharge correction using satellite altimetry-based discharge product, Hydrology and Earth System Sciences, 22, 2135–2162, https://doi.org/10.5194/hess-22-2135-2018, 2018.

Esteban Fernandez, D.: SWOT Project, Mission performance and error budget, Tech. rep., Jet Propulsion Laboratory, 2017.

Evensen, G.: Sequential data assimilation with a nonlinear quasi-geostropic model using Monte Carlo methods to forecast error statistics, Journal of Geophysical Research, 99, 10 143–10 162, https://doi.org/10.1029/94JC00572, 1994.

Evensen, G.: Advanced data assimilation for strongly nonlinear dynamics, Monthly Weather Review, 125, 1342–1354, https://doi.org/10.1175/1520-0493(1997)125<1342:ADAFSN>2.0.CO;2, 1997.

Evensen, G.: The Ensemble Kalman Filter: theoretical formulation and practical implementation, Ocean Dynamics, 53, 343–367, https://doi.org/10.1007/s10236-003-0036-9, 2003.

Evensen, G.: Sampling strategies and square root analysis schemes for the EnKF, Ocean Dynamics, 54, 539–560, https://doi.org/10.1007/s10236-004-0099-2, 2004.

Evensen, G. and Leeuwen, P. V.: An ensemble kalman smoother for nonlinear dynamics, Monthly Weather Review, 128, 1852–1867, https://doi.org/10.1175/1520-0493(2000)128<1852:AEKSFN>2.0.CO;2, 2000.

Fj´ortoft, R., Gaudin, J.-M., Pourthie, N., Lalaurie, J.-C., Mallet, A., Nouvel, J.-F., Martinot-Lagarde, J., Oriot, H., Borderies, P., Ruiz, C., and Daniel, S.: KaRIn on SWOT: Characteristics of near-nadir Ka-band interferometric SAR imagery, IEEE Transactions on Geoscience and Remote Sensing, 52, 2172–2185, https://doi.org/10.1109/TGRS.2013.2258402, 2014.

Guillet, O., Weaver, A., Vasseur, X., Michel, M., Gratton, S., and Gürol, S.: Modelling spatially correlated observation errors in variational data assimilation using a diffusion operator on an unstructured mesh, Quarterly Journal of the Royal Meteorological Society, in revision, 2018.

Gupta, H. V., Sorooshian, S., and Yapo, P. O.: Toward improved calibration of hydrological models: multiple and noncommensurable measures of information, Water Resources Research, 34, 751–763, https://doi.org/10.1029/97WR03495, 1998.

Hafliger, V., Martin, E., Boone, A., Ricci, S., and Biancamaria, S.: Assimilation of synthetic SWOT river depths in a regional hydrometeorological model, Water, 11, https://doi.org/10.3390/w11010078, 2019.

Hunt, B., Kalnay, E., Kostelich, E. J., Ott, E., Patil, D. T., Sauer, T., Szunyogh, I., Yorke, J. A., and Zimin, A. V.: Four-dimensional ensemble Kalman filtering, Tellus, 56, 273–277, https://doi.org/10.1111/j.1600-0870.2004.00066.x, 2004.

Hunt, B. R., Kostelich, E. J., and Szunyogh, I.: Efficient data assimilation for spatiotemporal chaos: A local ensemble transform Kalman filter, Physica D, 230, 112–126, https://doi.org/10.1016/j.physd.2006.11.008, 2007.

International Association of Hydrological Sciences Ad Hoc Group on Global Water Sets, Vörösmarty, C., Askew, A., Grabs, W., Barry, R. G., Birkett, C., Döll, P., Goodison, B., Hall, A., Jenne, R., Kitaev, L., Landwehr, J., Keeler, M., Leavesley, G., Schaake, J., Strzepek, K., Sundarvel, S. S., Takeuchi, K., and Webster, F.: Global water data: a newly endangered species, Eos. Trans. AGU, 82, 54–58, https://doi.org/10.1029/01EO00031, 2001.

Kurtz, W., Hendricks-Frassen, H.-J., and Vereecken, H.: Identification of time-variant river bed properties with Ensemble Kalman Filter, Water Resources Research, 48, https://doi.org/10.1029/2011WR011743, 2012.

Leeuwen, P. V. and Evensen, G.: Data assimilation and inverse methods in terms of a probabilistic formulation, Monthly Weather Review, 124, 2898–2913, https://doi.org/10.1175/1520-0493(1996)124<2898:DAAIMI>2.0.CO;2, 1996.

Liu, Y. and Gupta, H. V.: Uncertainty in hydrological modeling: Towards an integrated data assimilation framework, Water Resources Research, 43, https://doi.org/10.1029/2006WR005756, 2007.

Liu, Y., Weerts, A. H., Clark, M., Hendricks Franssen, H.-J., Kumar, S., Moradkhani, H., Seo, D.-J., Schwanenberg, D., Smith, P., van Dijk, A. I. J. M. N., van Velzen, N., He, M., Lee, H., Noh, S. J., Rakovec, O., and Restrepo, P.: Advancing data assimilation in operational hydrologic forecasting: progress, challenges, and emerging opportunities, Hydrology and Earth System Sciences, 16, 3863–3887, https://doi.org/10.5194/hess-16-3863-2012, 2012.

Maidment, D. R.: Handbook of hydrology, McGraw Hill Professional, 1993.

Manning, R.: On the flow of water in open channels and pipes, Institution of Civil Engineers of Ireland, 20, 161–207, 1891.

Meade, R., Rayol, J., Conceição, S. D., and Natividade, J.: Backwater Effects in the Amazon River Basin of Brazil, Environmental Geology and Water Sci., 18, 105–114, https://doi.org/10.1007/BF01704664, 1991.

Melsen, L., Teuling, A., Torfs, P., Zappa, M., Mizukami, N., Clark, M., and Uijlenhoet, R.: Representation of spatial and temporal variability in large-domain hydrological models: case study for a mesoscale pre-Alpine basin, Hydrology and Earth System Sciences, 20, 2207–2226, https://doi.org/10.5194/hess-20-2207-2016, 2016.

Mersel, M. K., Smith, L. C., Andreadis, K. M., and Durand, M. T.: Estimation of river depth from remotely-sensed hydraulic relationship, Water Resources Research, 49, 3165–3179, https://doi.org/10.1002/wrcr.20176, 2013.

Michailovsky, C. I., Milzow, C., and Bauer-Gottwein, P.: Assimilation of radar altimetry to a routing model of the Brahmaputra river, Water Ressources Research, 49, 4807–4816, https://doi.org/10.1002/wrcr.20345, 2013.

Molinier, M., Guyot, J.-L., Orstom, B., Guimarães, V., de Oliveira, E., and Dnaee, B.: Hydrologie du bassin de l'Amazone, in: Grands Bassins Fluviaux Périatlantiques, edited by Editions, O., pp. 335–345, PEGI-INSA-CNRS-ORSTOM, Paris, 1993.

Montzka, C., Moradkhani, H., Weihermüller, L., Hendricks-Franssen, H.-J., Canty, M., and Vereecken, H.: Hydraulic parameter estimation by remotely-sensed top soil moisture observations with the particle filter, Journal of Hydrology, 399, 410–421, https://doi.org/10.1016/j.jhydrol.2011.01.020, 2011.

Moradkhani, H., Hsu, K.-L., Gupta, H., and Sorooshian, S.: Uncertainty assessment of hydrologic model states and parameters: Sequential data assimilation using particle filter, Water Resources Resaerch, 41, https://doi.org/10.1029/2004WR003604, 2005.

Noilhan, J. and Planton, S.: A simple parameterization of land surface processes for meteorological models, Mon. Wea. Rev., 117, 536–549, https://doi.org/10.1175/1520-0493(1989)117<0536:ASPOLS>2.0.CO;2, 1989.

Oki, T. and Sud, Y. C.: Design of Total Integrating Pathways (TRIP)-A Global River Channel Network, Earth Interactions, 2, 1–36, https://doi.org/10.1175/1087-3562(1998)002<0001:DOTRIP>2.3.CO;2, 1998.

Ott, E., Hunt, B. R., Szunyogh, I., Kostelich, A. V. Z. A. J., Corazza, M., Kalnay, E., Patil, D. J., and Yorke, J. A.: A local ensemble Kalman filter for atmospheric data assimilation, Tellus A, 56, 415–428, https://doi.org/10.1111/j.1600-0870.2004.00076.x, 2004.

Oubanas, H., Gejadze, I., Malaterre, P.-O., Durand, M., Wei, R., Frasson, R. P. M., and Domeneghetti, A.: Discharge estimation in ungauged basins through variational data assimilation: the potential of the SWOT mission, Water Resources Research, 54, https://doi.org/10.1002/2017WR021735, 2018.

Paiva, R. C. D., Buarque, D. C., Collischonn, W., Bonnet, M.-P., Frappart, F., Calmant, S., and Mendes, C. A. B.: Large scale hydrological and hydrodynamic modeling of the Amazon River basin, Water Resources Research, 49, 1226–1243, https://doi.org/10.1002/wrcr.20067, 2013.

Panzeri, M., Riva, M., Guadagnini, A., and Neuman, S. P.: Data assimilation and parameter estimation via ensemble kalman filter coupled with stochastic moment equations of transient groudwater flow, Water Resources Research, 49, 1334–1344, https://doi.org/10.1002/wrcr.20113, 2013.

Pathiraja, S., Marshall, L., Sharma, A., and Moradkhani, H.: Detecting non-stationar hydrologic model parameters in a paired catchment system using data assimilation, Advances in Water Resources, 94, 103–119, https://doi.org/10.1016/j.advwatres.2016.04.021, 2016.

Pedinotti, V., Boone, A., Ricci, S., Biancamaria, S., and Mognard, N.: Assimilation of satellite data to optimize large-scale hydrological model parameters: a case study for the SWOT mission, Hydrology and Earth System Science, 18, 4485–4507, https://doi.org/10.5194/hess-18-4485-2014, 2014.

Rakovec, O., Weerts, A. H., Sumihar, J., and Uijlenhoet, R.: Operational aspects of asynchronous filtering for flood forecasting, Hydrology and Earth System Sciences, 19, 2911–2924, https://doi.org/10.5194/hess-19-2911-2015, 2015.

Renard, B., Kavetski, D., Kuczera, G., Thyer, M., and Franks, S. W.: Understanding predictive uncertainty in hydrologic modeling: the challenge of identifying input and structural errors, Water Resources Research, 46, https://doi.org/10.1029/2009WR008328, 2010.

Rodell, M., Beaudoing, H. K., L'Ecuyer, T. S., Olson, W. S., Famiglietti, J. S., Houser, P. R., Adler, R., Bosilovich, M. G., Clayson, C. A., Chambers, D., Clark, E., Fetzer, E. J., Gao, X., Gu, G., Hilburn, K., Huffman, G. H., Lettenmaier, D. P., Liu, W. T., Roberton, F. R., Schlosser, C. A., Sheffield, J., and Wood, E. F.: The observed state of the water cycle in the early twenty-first century, Journal of Climate, 28, 8289–8318, https://doi.org/10.1175/JCLI-D-14-00555.1, 2015.

Ruiz, J. J., Pulido, M., and Miyoshi, T.: Estimating model parameters with ensemble-based data assimilation, Journal of the Meteorological Society of Japan, 91, 79–99, https://doi.org/10.2151/jmsj.2013-201, 2013.

Sakov, P., Evensen, G., and Bertino, L.: Asynchronous data assimilation with the EnKF, Tellus, 62, 24–29, https://doi.org/10.1111/j.1600-0870.2009.00417.x, 2010.

Sanoo, A. K., Pan, M., Troy, T. J., Vinukollu, R. K., Sheffield, J., and Wood, E. F.: Reconciling the global terrestrial water budget using satellite remote sensing, Remote Sensing of Environment, 115, 1850–1865, https://doi.org/10.1016/j.rse.2011.03.009, 2011.

Shi, Y., Davis, K. J., Zhang, F., Duffy, C. J., and Yu, X.: Parameter estimation of physically-based land surface model hydrologic model using an ensemble Kalman filter: a multivariate real-data experiment, Advances in Water Resources, 83, 421–427, https://doi.org/10.1016/j.advwatres.2015.06.009, 2015.

Silva, J. S. D., Calmant, S., Seyler, F., Filho, O. C. R., Cochonneau, G., and Mansur, W. J.: Water levels in the Amazon basin derived from the ERS 2 and ENVISAT radar altimetry missions, Remote Sensing of Environment, 114, 2160–2181, https://doi.org/10.1016/j.rse.2010.04.020, 2010.

Sood, A. and Smakhtin, V.: Global hydrological models: a review, Hydrological Sciences Journal, 60, 549–565, https://doi.org/10.1080/02626667.2014.950580, 2015.

Talagrand, O. and Courtier, P.: Variational assimilation of meteorological observations with the adjoint vorticity equation, Part 1: Theory, Quarterly Journal of the Royal Meteorological Society, 113, 1311–1328, https://doi.org/10.1002/qj.49711347812, 1987.

Vinukollu, R. K., Meynadier, R., Sheffield, J., and Wood, E. F.: Multi-model, multi-sensor esti- mates of global evapotranspiration : climatology, uncertainties and trents, Hydrological Processes, 25, 3993–4010, https://doi.org/10.1002/hyp.8393, 2011.

Vrugt, J. A., ter Braak, C. J. F., Diks, C. G. H., and Shoups, G.: Hydrological data assimilation using particle Markov chain Monte Carlo simulation: Theory, concepts and applications, Advances in Water Resources, 51, 457–478, https://doi.org/10.1016/j.advwatres.2012.04.002, 2012.

Wisser, D., Feketa, B., Vörösmarty, C. J., and Schumann, A. H.: Reconstructing 20th century global hydrography: a contribution to the Global Terrestrial Network- Hydrology (GTN-H), Hydrology and Earth System Sciences, 14, 1–24, https://doi.org/10.5194/hess-14-1-2010, 2010.

Yoon, Y., Durand, M., Merry, C. J., Clark, E. A., Andreadis, K. M., and Alsdorf, D. E.: Estimating river bathymetry from data assimilation of synthetic SWOT measurements, Journal of Hydrology, 464-465, 363–375, https://doi.org/10.1016/j.jhydrol.2012.07.028, 2012.
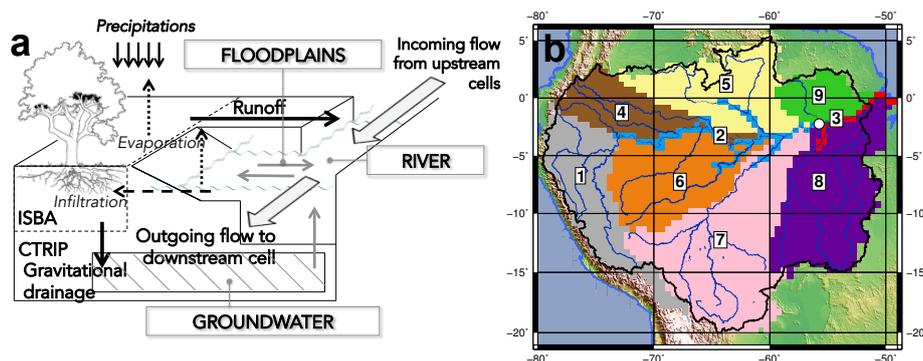
**Figure 1.** (a) The ISBA-CTRIP system for a given grid cell. ISBA surface runoff ($Q_{\mathrm{ISBA,sur}}$) flows into the river/surface reservoir $S$, ISBA gravitational drainage ($Q_{\mathrm{ISBA,sub}}$) feeds groundwater reservoir $G$. The surface water is transferred from one cell to another following the TRIP river routing network. (b) Hydro-geomorphological areas of the Amazon basin from Emery et al. (2016) with the gauge of Óbidos located by the white circle at the entry of the zone 3.
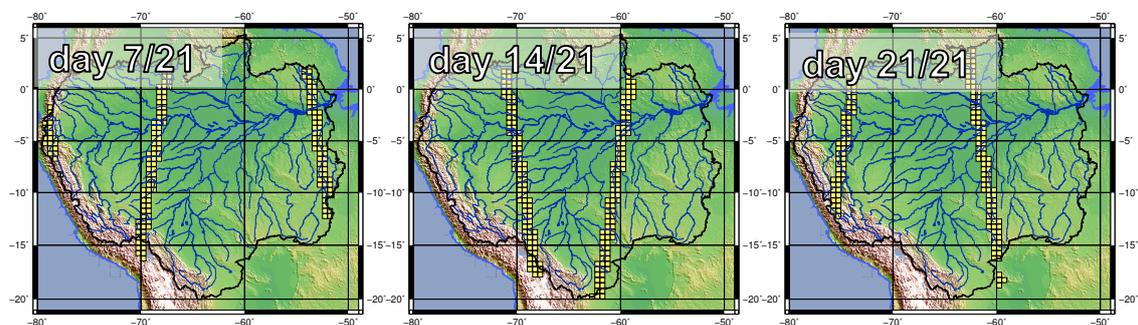
**Figure 2.** SWOT swaths at ISBA-CTRIP resolution over the Amazon basin.
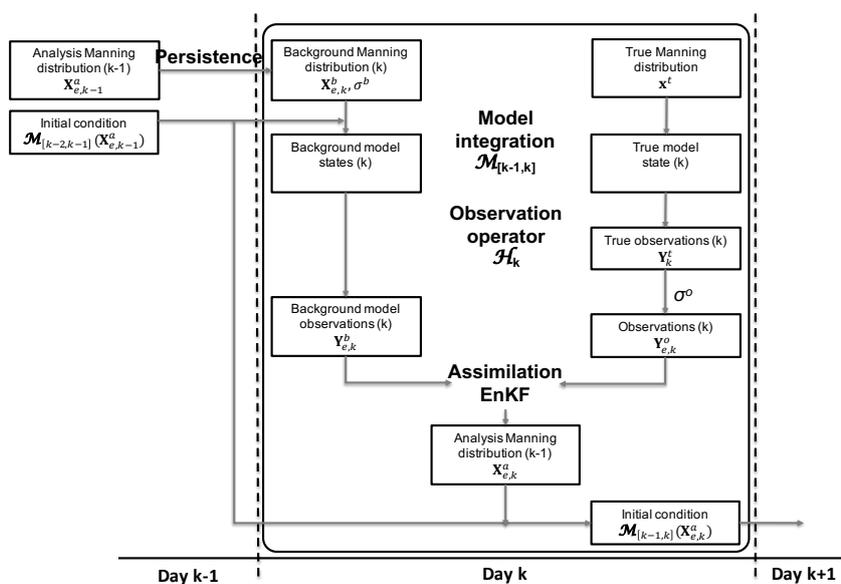
**Figure 3.** Data assimilation framework over the assimilation cycle $[k-1,\ k]$ including (1) a forecast step to integrate the ensemble of ISBA-CTRIP simulations, each member having a different spatially-distributed Manning coefficient, (2) an analysis step to correct this ensemble of Manning coefficients using synthetic observations through the Kalman filter equation and (3) re-run the ISBA-CTRIP model with these analysis estimates to obtain the updated model states.
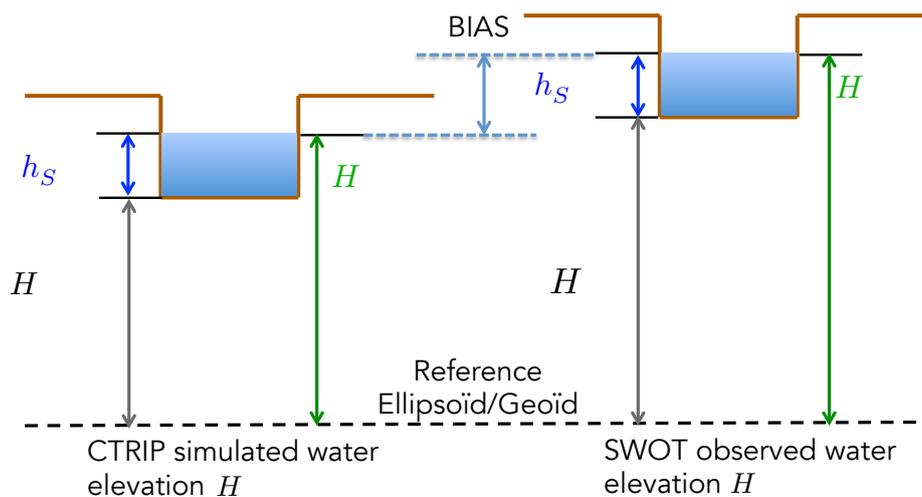
**Figure 4.** Illustration of a bias case between the water elevation as observed by SWOT ($H_{\mathrm{alti}}^{\mathrm{SWOT}}$) and the one simulated by CTRIP ($H_{\mathrm{alti}}^{\mathrm{TRIP}}$) because of a bias between model and true river beds.
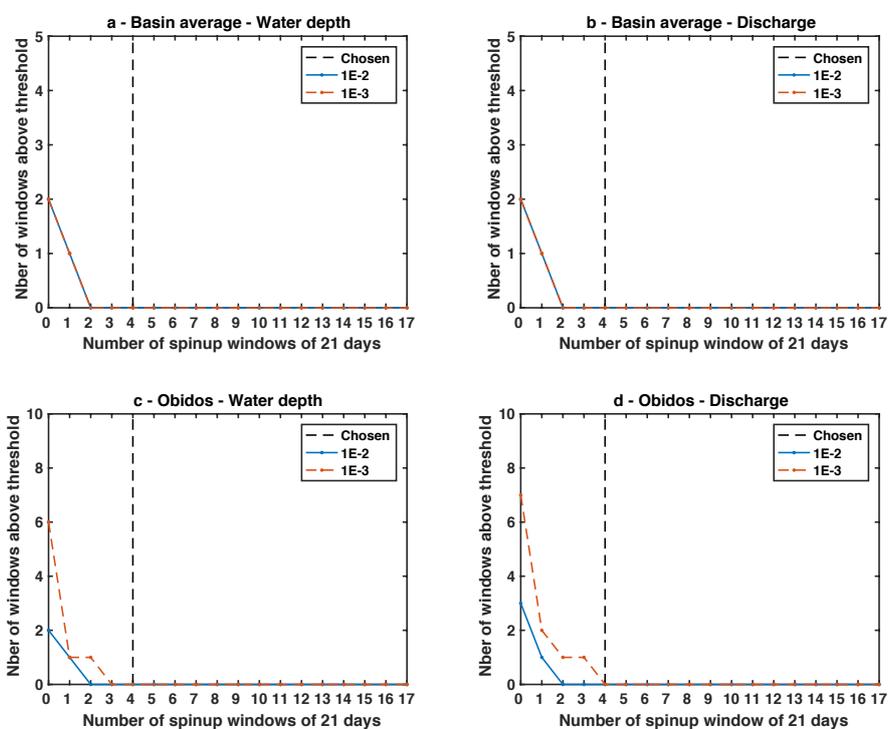
**Figure 5.** Results for the spinup sensitivity test. Each test run is represented along the $x$-axis and referenced by its number of spinup windows. The $y$-axis displays the number of windows during which the relative difference between the true run and the openloop run in which the Manning spatial distribution is modified is above the chosen threshold. These statistics are obtained for the discharge (a,c) and the water depth (b,d) and evaluated over the entire basin (a,b) and at the downstream station of Óbidos (c,d). Note that the vertical dashed line corresponds to the minimum model spinup period retained in this study.
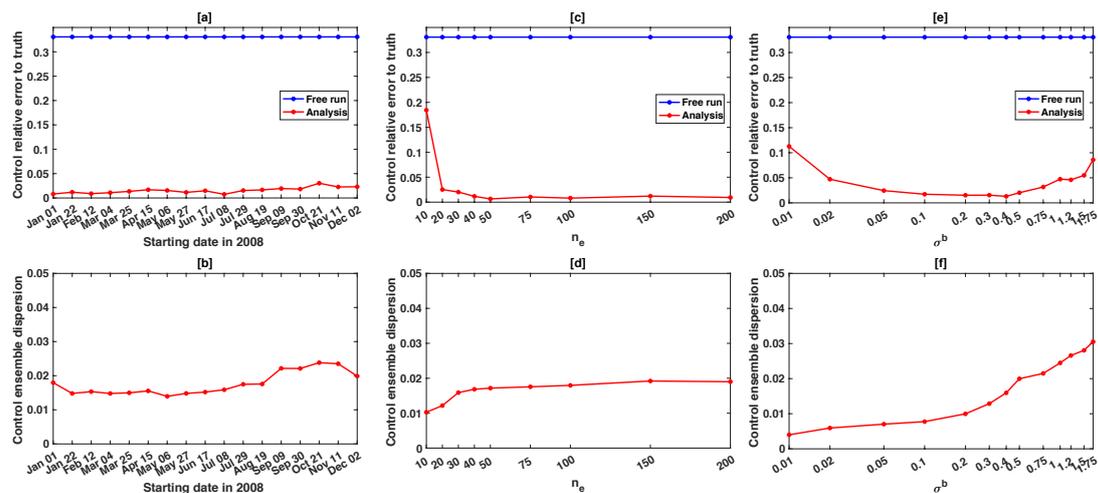
**Figure 6.** (Top) Relative error (to the truth) and (Bottom) dispersion of the analysis control ensemble (averaged over all control variables) for the sensitivity tests to (a-b) the data assimilation starting date, (c-d) the ensemble size $n_e$, (e-f) the background error standard deviation $\sigma^b$. For each test, a set of one-cycle-long data assimilation experiments is run.
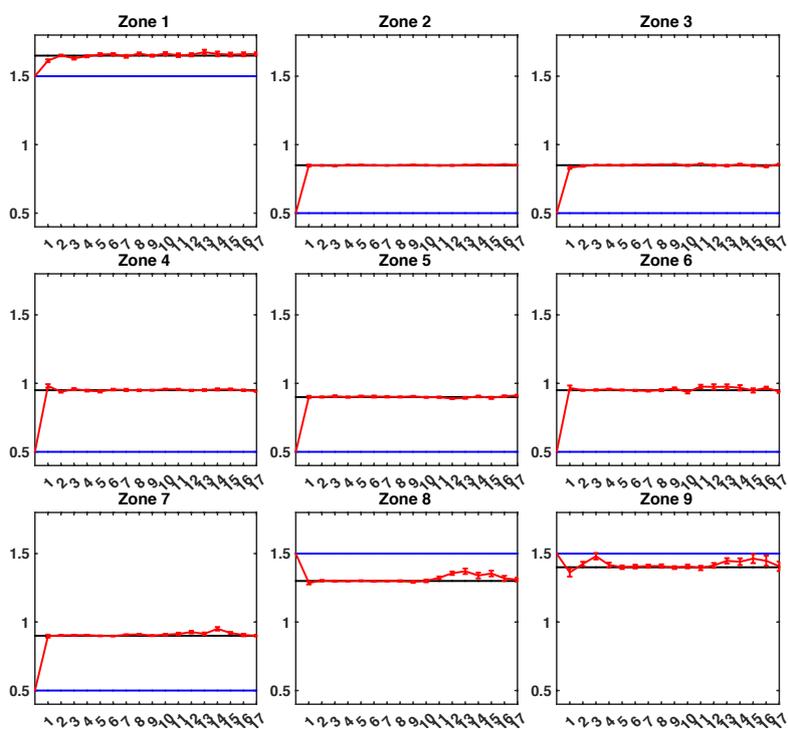
**Figure 7.** Control variables assimilation results for the PE1 experiment: evolution of the ensemble-averaged analysis control variable (red line) for each zone (one zone per subplot) with respect to the assimilation cycle and compared to the corresponding true value (black line) and the openloop value (blue line).
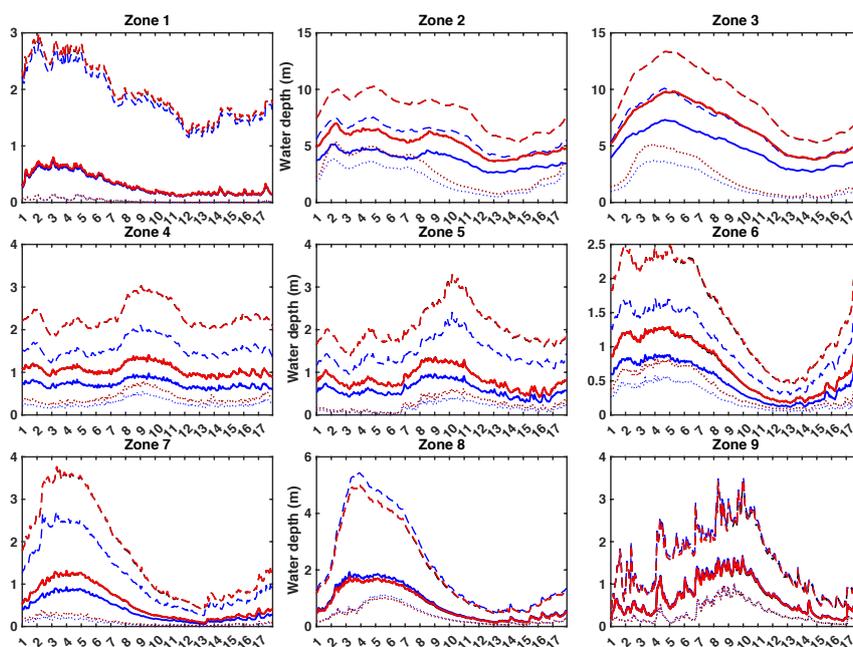
**Figure 8.** Water depths assimilation results for the PE1 experiment: daily evolution of the ensemble-averaged analysis water depth (red lines) compared to the true water depths (black lines) and the openloop water depths (blue line). For each zone (one per subplot), the median (full line), the first decile (dotted line) and the ninth decile (dashed line) of water depth ensemble over all grid cells in the zone are represented.
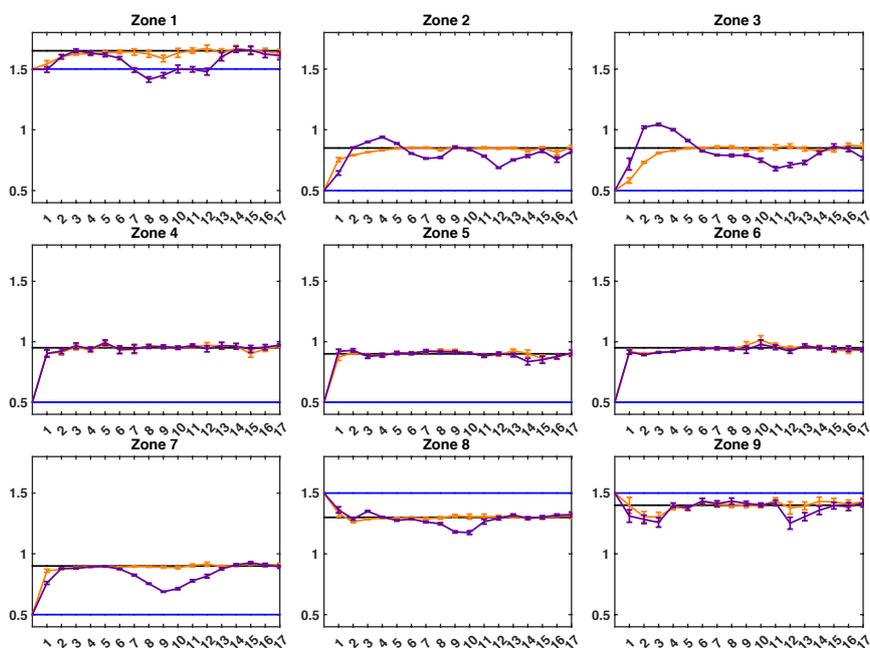
**Figure 9.** Control variables assimilation results for the PE2 and PE3 experiments: evolution of the ensemble-averaged analysis control variable for the PE2 experiment (orange line) and the PE3 experiment (purple line) for each zone (one zone per subplot) with respect to the assimilation cycle and compared to the corresponding true value (black line) and the openloop value (blue line).
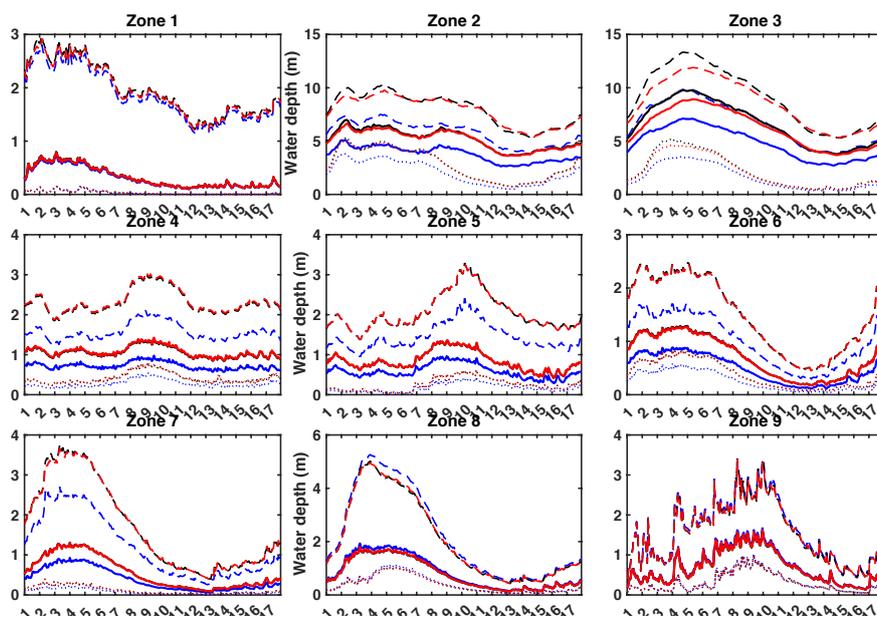
**Figure 10.** Water depths assimilation results for the PE3 experiment: daily evolution of the ensemble-averaged analysis water depth (red lines) compared to the true water depths (black lines) and the openloop water depths (blue line). For each zone (one per subplot), the median (full line), the first decile (dotted line) and the ninth decile (dashed line) of water depth ensemble over all grid cells in the zone are represented.

| Parameter | Nb run | Range |
|:---:|:---:|:---:|
| Spinup | 18 | From 0 window to 17 windows of 21 days |
| Starting date | 17 | Starting January 1st, 2008 and on, every 21 days |
| $n_e$ | 9 | [ 10 20 30 40 50 75 100 150 200 ] |
| $\sigma^b$ | 13 | [ 0.01 0.02 0.05 0.1 0.2 0.3 0.4 0.5 0.75 1.0 1.2 1.5 1.75 ] |

**Table 1.** Tested data assimilation parameters in the sensitivity tests.

| Simulation name | Observation variables | Bathymetry bias |
|:---:|:---:|:---:|
| PE1 | Water depths | No |
| PE2 | Water depth anomalies | No |
| PE3 | Water depth anomalies | Yes |

**Table 2.** List of data assimilation experiments. All experiments are run over approximately one year (17 cycles of 21 days) starting on January 1st, 2008. The ensemble size is $n_e = 25$, the observation error standard deviation is $\sigma^o = 0.1$ m and the initial control variable error standard deviation is $\sigma^b = 0.3$.

| Run | Starting date | Manning distr. change | Spinup length (in wdws of 21 days) |
|---|---|---|---|
| Reference | Dec 16, 2006 | - | 18 (=378 days) |
| 1 | Dec 16, 2006 | Jan 09, 2007 | 17 (=357 days) |
| 2 | Dec 16, 2006 | Jan 30, 2007 | 16 (=336 days) |
| 3 | Dec 16, 2006 | Feb 20, 2007 | 15 (=315 days) |
| 4 | Dec 16, 2006 | Mar 13, 2007 | 14 (=294 days) |
| 5 | Dec 16, 2006 | Apr 03, 2007 | 13 (=273 days) |
| 6 | Dec 16, 2006 | Apr 24, 2007 | 12 (=252 days) |
| 7 | Dec 16, 2006 | May 15, 2007 | 11 (=231 days) |
| 8 | Dec 16, 2006 | Jun 05, 2007 | 10 (=210 days) |
| 9 | Dec 16, 2006 | Jun 26, 2007 | 9 (=189 days) |
| 10 | Dec 16, 2006 | Jul 17, 2007 | 8 (=168 days) |
| 11 | Dec 16, 2006 | Aug 07, 2007 | 7 (=147 days) |
| 12 | Dec 16, 2006 | Aug 28, 2007 | 6 (=126 days) |
| 13 | Dec 16, 2006 | Sept 18, 2007 | 5 (=105 days) |
| 14 | Dec 16, 2006 | Oct 09, 2007 | 4 (=84 days) |
| 15 | Dec 16, 2006 | Oct 30, 2007 | 3 (=63 days) |
| 16 | Dec 16, 2006 | Nov 20, 2007 | 2 (=42 days) |
| 17 | Dec 16, 2006 | Dec 11, 2007 | 1 (=21 days) |
| 18 | Dec 16, 2006 | Jan 01, 2008 | 0 (=0 days) |

**Table 3.** Spinup sensitivity test set up: each run consists in an approximately-two-year-long ISBA-CTRIP run starting on Dec 16, 2006 (column 2) and ending on Dec 22, 2008. After a given number of 21-day windows during the first year (column 3), the Manning distribution is changed to replicate an assimilation update step while the reference run (row 2) used the same Manning for the entire run. The period between the instant when the Manning distribution is changed and the beginning of the second year of simulation corresponds to the spinup period (column 4). The simulated water depth/discharge during the second year of run are then compared to the reference run to evaluate the impact of the spin up.
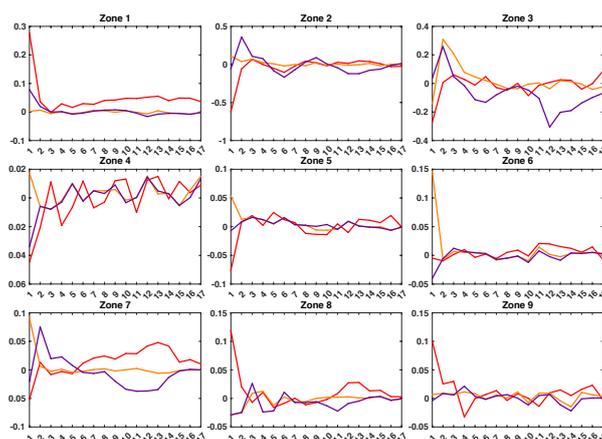
**Figure A1.** Evolution of the EnKF innovations ($"\left(\mathbf{y}_k^{o,[l]} - \mathcal{H}_k\left(\mathbf{x}_k^{b,[l]}\right)\right)"$ term in Eq. 12) with respect to the assimilation cycle for PE1 (red line), PE2 (orange line) and PE3 (purple line). For each zone (one zone per subplot), the displayed innovation is the averaged of all the innovations in the corresponding zones.